MHD MATERIALS - SEED/SLAG INTERACTIONS AND EFFECTS

QUARTERLY PROGRESS REPORT

July 1 - September 30, 1980

Samuel J. Schneider
Project Manager

Center for Materials Science
U. S. Department of Commerce
National Bureau of Standards
Washington, D. C. 20234

PREPARED FOR THE UNITED STATES
DEPARTMENT OF ENERGY
MHD OFFICE

MHD MATERIALS - SEED/SLAG INTERACTIONS AND EFFECTS

QUARTERLY PROGRESS REPORT

July 1 - September 30, 1980

Samuel J. Schneider
Project Manager

Center for Materials Science
U. S. Department of Commerce
National Bureau of Standards
Washington, D. C. 20234

PREPARED FOR THE UNITED STATES
DEPARTMENT OF ENERGY
MHD OFFICE

TABLE OF CONTENTS

I. SUMMARY OF PROGRESS TO DATE

1. Thermochemistry of Seed and Slag

Vapor pressure data of K over K_2O-CaO-Al_2O_3-SiO_2 samples are reported and compared. The K pressure at equal K_2O and CaO concentrations is insensitive to variation in the Al_2O_3 and SiO_2 concentration (probably within limits) if the sum of the Al_2O_3 and SiO_2 concentrations are constant. The K_2O activity of two samples at equal K_2O concentrations, is reduced by increased Al_2O_3 + SiO_2 concentration and reduced CaO concentration, but remains proportional at varying K_2O concentrations.

Phase equilibria studies along the join K_2CO_3-$KAlO_2$ have pointed to the possibility of high temperature mesomorphic ("liquid crystal") behavior. Also, as a supplement to experimental work in the system K_2O-CaO-Al_2O_3-SiO_2, liquidus diagrams have been calculated for selected binary joins. These calculations reaffirm the marked non-ideality of most silicate solutions with respect to molecular end members and point up the need for accurate models of K_2O-CaO-Al_2O_3-SiO_2 melts.

2. Electrical Conductivity and Polarization

Four probe AC electrical conductivity measurements are compared with four probe DC measurements on slag from a coal burning steam plant in Bow, NH. AC and DC data agree quite well with some anomalies existing over the temperature range measured. The measurements support the suggestion made in previous reports that above 1385 °C, ionic conductivity is the predominant transport mechanism in this particular slag which contains a relatively large amount of iron.

3. Corrosion of Downstream Components

Type 316 stainless steel tubes were exposed to an oxygen-rich and fuel-rich environment seeded with K_2SO_4 and K_2CO_3. The samples were maintained at 500 °C and 590 °C wall temperature using internal air cooling. SEM and EDX analysis was performed on sections of the samples showing the chemical nature of the reaction zone and salt deposit. As seen in previous experiments the Fe penetrates the salt deposit to the greatest extent followed by lesser penetration by Cr while Ni is sometimes found in the metal at the interface. In the coming quarter the plans are to continue the study of Type 316 stainless steels using SEM-EDX analysis and to collect and analyze x-ray diffraction data on residue salt deposit material from fuel-rich and oxygen-rich system. Also, the feasibility of using metal and ceramic coatings on mild steel (with the testing of specific materials at 590 °C) will be examined.

II. DETAILED DESCRIPTION OF TECHNICAL PROGRESS

1. Thermochemistry of Seed and Slag (E. R. Plante and L. P. Cook)

Progress:

A. Vaporization Studies (E. Plante)

Measurements of the K and O_2 vapor pressures over a third sample in the K_2O-CaO-Al_2O_3-SiO_2 system were completed. These data were obtained using a Knudsen-effusion, modulated beam mass spectrometric method. The objective of these measurements is to produce sufficient experimental results to provide a data base for the construction of a simple empirical model for prediction of alkali seed retention of real slags produced by combustion of Western sub-bituminous coals in an MHD seeded environment.

Previous reports have described and compared the potassium pressure measurements on a K_2O-Al_2O_3-SiO_2 composition in the absence of CaO with results obtained on two K_2O-CaO-Al_2O_3-SiO_2 samples. These results showed that calcia has a major effect on K_2O retention and increases the K_2O activity by orders of magnitude at calcia concentrations which would be characteristic of Western slags obtained by combustion of Western coals (for example, Rosebud) in a seeded MHD combustion process.

This report includes new data obtained on a third K_2O-CaO-Al_2O_3-SiO_2 model slag. As in the previous work, this slag model is based on the 4 component phase diagram and has been selected so that the initial composition lies close to an invariant melting point. We believe that such compositions will tend to give rise to liquid solutions which will have vaporization properties similar to slag solutions once melting has taken place. Later work will be extended to include compositions in which one or more solid phases may be present.

Table 1 lists the sample designations, mineral components and starting composition for the 3 model slag systems studied to date.

The CaO concentrations in KCAS-VP-1 and KCAS-VP-3 are 27.5 and 28.0 wt% respectively and the observed K pressures at equal K_2O concentrations agree within reasonable experimental error (certainly ±30 percent). This is true despite the changes in the Al_2O_3 and SiO_2 concentrations which are 22.2 and 35.5 wt% respectively for the KCAS-VP-1 sample and 13.5 and 46.0 wt% respectively for the KCAS-VP-3 sample. This indicates that within a limited composition range, Al_2O_3 and SiO_2 can be interchanged on a wt% basis with essentially no effect on the K_2O activity. Comparison of the K pressures of KCAS-VP-2 and KCAS-VP-3 at equal K_2O concentrations shows that the KCAS-VP-3 pressures are about 2.3 times as great as the KCAS-VP-2 pressures independent of the K_2O concentration. This difference is attributed to the lower calcia content of the KCAS-VP-2 sample but part of the effect may also be due to the higher Al_2O_3 + SiO_2 concentration.

These results are illustrated in figure 1-a which shows the K pressure as a function of wt% K_2O at a temperature of 1667 K. The points for the KCAS-VP-1 and KCAS-VP-2 data were calculated at the average K_2O concentrations from the least squares constants listed in Table 2 while the curve for KAS-VP-3 was obtained from a fit of the data to an equation assuming a linear dependence of log P_k on the wt% K_2O in the sample.

Table 2 lists experiment identification, K_2O concentration range, the slope and its standard error, and the intercept and its standard error when the K pressure is fit to the equation:

$$\log P = A/T + B.$$

Generally the observed slopes are in reasonably good agreement except for the initial data for each sample. The initial data in each series is subject to more error due to evaporation of unreacted starting materials such as unreacted K_2CO_3 and is believed, therefore, to be less reliable. The initial data in the KCAS-VP-1 series shows slopes which are more characteristic of evaporation of K from $KAlSiO_4$ than from slag solutions. This may possibly be due to having a sample which is somewhat off-composition.

Table 1

Mineral Constituents and Composition of Vaporization Samples

Sample	Mineral Constituents (Wt%)	Composition Wt% K_2O	CaO	Al_2O_3	SiO_2
KCAS-VP-1	$KAlSiO_4$ (49.8), Ca_2SiO_4 (16.5) $Ca_2Al_2SiO_7$ (16.5), $Ca_3Si_2O_8$ (17.2)	14.8	27.5	22.2	35.5
KCAS-VP-2	$KAlSiO_4$ (28.6), $KAlSi_2O_6$ (13.8) $Ca_2Al_2SiO_7$ (28.9), $CaAl_2Si_2O_8$ (28.7)	11.5	17.6	33.7	37.2
KCAS-VP-3	$KAlSiO_4$ (42.0), $CaSiO_3$ (58.0)	12.5	28.0	13.5	46.0

Table 2

Slope, Intercept and Standard Deviations for K Pressure Data

Expt Id	Wt% K_2O	A	σ A	B	σ B
KCAS-VP-1					
3-13-80	14.8-12.4	-20047	391	8.144	.255
3-14-80	12.4-9.3	-19071	524	7.278	.334
3-18-80	9.3-7.2	-17429	452	6.058	.289
3-18-80	6.2-4.8	-16372	210	5.068	.129
3-21-80	4.8-4.0	-16896	279	5.289	.178
KCAS-VP-2					
5-14-80	11.4-10.7	-14632	434	4.200	.278
5-15-80	10.7-8.6	-16366	180	5.097	.112
5-16-80	8.6-6.5	-17571	257	5.656	.158
5-19-80	6.5-6.2	-16606	526	4.992	.321
KCAS-VP-3					
8-13-80	12.5-10.8	-15052	775	4.983	.512
8-14-80	10.8-10.3	-17512	453	6.282	.298
8-14-80	10.3-7.4	-15441	612	4.732	.374
8-15-80	7.4-6.0	-16006	581	5.178	.362
8-15-80	6.0-3.9	-15390	320	4.544	.197
8-18-80	3.9-3.2	16948	801	5.417	.505

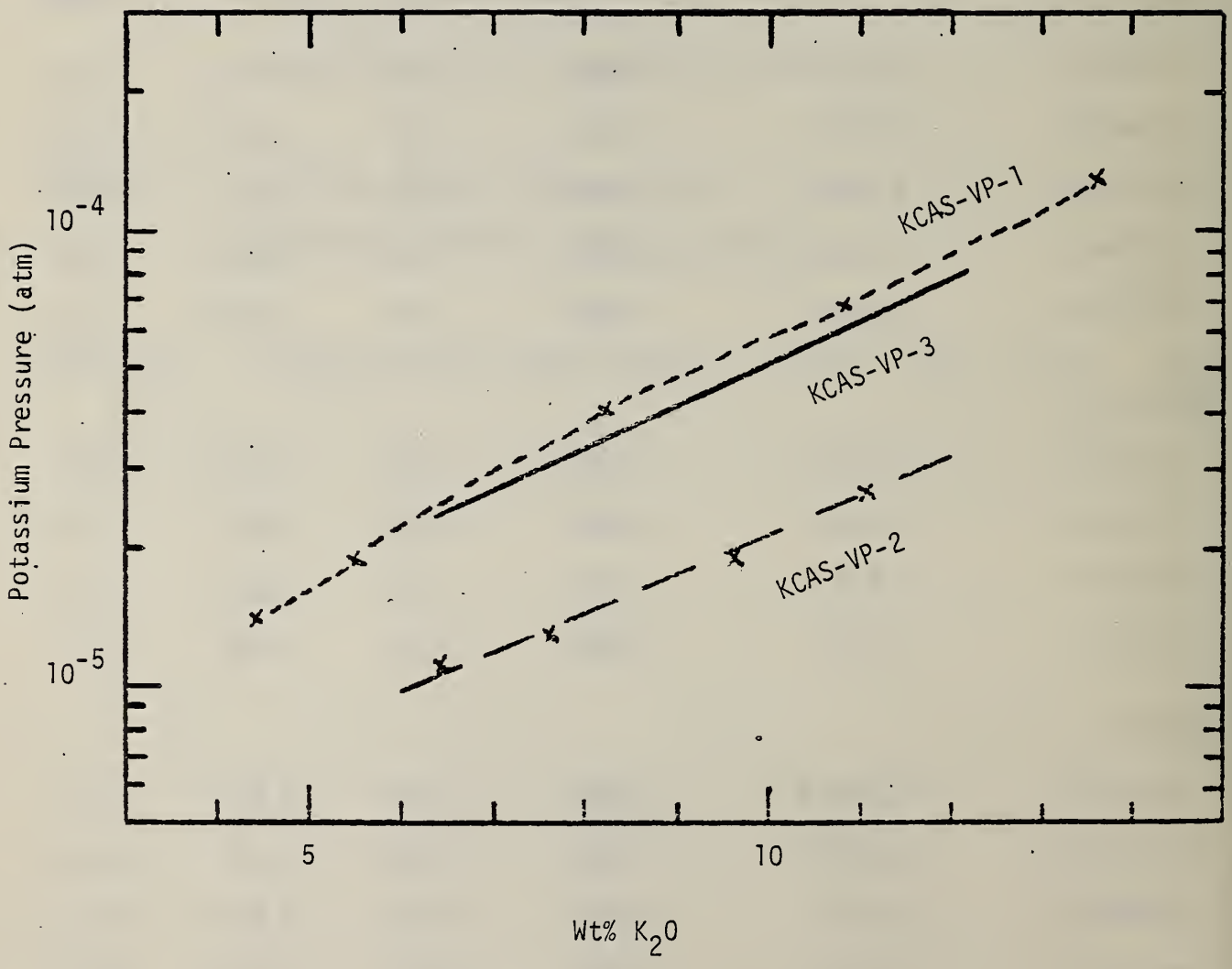

Figure 1-a Potassium pressure as a function of K_2O concentration for 3 samples in the K_2O-CaO-Al_2O_3-SiO_2 system at 1667.K.

B. Phase Equilibria (L. Cook)

Progress:

1. K_2CO_3-$KAlO_2$

Phase equilibrium behavior in the more K_2O-rich parts of the system K_2O-CaO-Al_2O_3-SiO_2 is comparatively complex as outlined in the previous three quarterly reports. During the past quarter, an attempt was made to resolve the nature of the complex interaction between potassium carbonate and potassium aluminate. Potassium carbonate, added as seed, is expected to be an important phase in all MHD systems except possibly those using the most sulfur-rich of coals. Potassium aluminate together with silica comprises by weight the most important component of MHD slag [1-3]. The carbonate/aluminate interaction, which is thought to be interfacially controlled is potentially of prime importance to the design and operation of downstream MHD components where the flow of slag and condensed seed phases must be predictable. A preliminary investigation showed a rather dramatic and surprising lack of evidence for flowage or wetting in certain K_2CO_3-rich mixtures at temperatures as high as 1300 °C. Initially this was thought to be due to formation of intermediate solid solutions. This troublesome phenomenon has been investigated further as follows.

Both K_2CO_3 and $KAlO_2$ are extremely hygroscopic, necessitating the use of special methods. Preparation, purity and handling procedures for these materials have been described in ref. [3]. X-ray analysis was completed on a powder diffractometer equipped with a dry cell and graphite monochromator using CuKα radiation. Additional characterization was done via a scanning electron microscope [SEM] with energy dispersive x-ray [EDX] analyzer.

Four principal types of experiment were performed on carefully homogenized K_2CO_3/$KAlO_2$ mixtures. In the first, 25 to 50 mg pellets of 6.4 mm dia. were pressed, dried at 800 °C, weighed and heated for 5-15 min. in a covered 15 ml Pt crucible at 1150 °C. After noting weight loss (always less than 10 percent), specimens were examined by x-ray, SEM and EDX. In the second type of experiment, powders were placed in a 2.6 mm i.d. Pt capsule with ends crimped loosely, which was in turn welded in a 4.6 mm i.d. Pt capsule. Capsules were then maintained at constant temperature for about one hour and quenched. By noting whether material was present in the outer capsule, melting or lack thereof could be determined, given the tendency of molten potassium carbonate to wet platinum. In the third type of experiment, several hundred mg of powder were placed in a Pt foil boat inside a covered 15 ml Pt crucible. This was heated in a muffle furnace, cooled in dry air, weighed and a portion was x-rayed. The remainder was reweighed and used for the continuation of the series of experiments, until all K_2CO_3 was vaporized. This took from 2-6 hours. The fourth type of experiment utilized a high temperature x-ray apparatus of the type described in ref. [4]. Because of weight loss problems associated with the presence of cold surfaces in this apparatus, it was necessary to use pressed pellets, introducing errors in the temperature measurement and the lattice parameters. Therefore, only qualitative observations could be made using the high temperature x-ray set-up.

Shown on Figure 1 are the conditions under which the four types of experiments were performed. A lack of melting is evident for compositions other than the most K_2CO_3-rich, as judged by the criteria of change in net shape of the sample and wetting of the Pt container. This is unexpected because of the known fluxing effect of K_2CO_3 and also because of the lack of reported high temperature compounds between K_2O or K_2CO_3 and $KAlO_2$.[1] Figure 1 also shows a calculated liquidus diagram assuming ideal solution behavior.[2] Copious melting would be expected for a large range of compositions via any reasonable liquidus diagram in the absence of intermediate compounds or solid solutions.

Information from the pellet experiments can be summarzied as follows. Potassium aluminate sinters readily in a short period of time to yield a dense pellet with few voids. Pellets of (K_2CO_3/$KAlO_2$) compositions 50/50, 60/40, 70/30, 80/20 and up to and including 90/10 retain their shape well (see Fig. 2-a) and become only very loosely bonded to the Pt foil, if at all, during the experiments. The outer surfaces in this composition range, especially those of the 90/10 composition (Fig. 2-b), show evidence of coarse crystallinity. From EDX examination, aluminum appears to be homogeneously distributed throughout. Voids are present in the interior of these pellets. Some evidence of reaction with platinum was noted which may be associated with a green color. Reaction with platinum is not necessarily the cause of the color, however. Platinum appears to be almost exclusively concentrated in small layered groups of platelets between the larger grains. It does not appear to be an important chemical constitutent of the major crystalline phase.

By contrast with the more $KAlO_2$-rich compositions, those in the range 92/08 to 100/0 show definite melting with extensive flowage and wetting of the Pt foil (Fig. 3). However, for the 92/08 specimen, the suggestion is of partial melting rather than complete melting: the melt has not coalesced into the corners of the foil, and there is extensive topographic development on the surface. Two types of surface can be discerned, one of which may represent crystallized melt (Fig. 4). The latter occurs in areas where obvious melting and flowage have occurred. This latter surface is apparently a manifestation of a definite structural arrangement, i.e., ordered intergrowths in the underlying K_2CO_3 lattice. A high surface tension is suggested by the curious features shown in Figure 5-a. Their origin appears to require a rather complicated explanation, but they are ubiquitous. The second type of surface in the 92/08 pellet experiment is illustrated in Figure 5-b. Sharp outlines and jagged surface topography suggest but do not prove crystallinity at the temperature of the experiment. Chemistry appears similar

---

[1] The synthesis of K_3AlO_3 has been reported in ref. [5], but this compound apparently cannot be synthesized using K_2CO_3 and may not be stable above 500-600 °C.

[2] Thermodynamic properties for K_2CO_3 used in this calculation have been obtained from ref. [6]. The melting point of $KAlO_2$ is from ref. [7], and its heat of fusion is from ref. [8].

to that of the bulk. An ordered arrangement of crystal platelets was usually apparent in these regions of the pellet. These platelets can be differentiated by their morphology from the Pt-rich phases noted above. In certain instances a suggestion of layering at right angles to the platelet axes can be seen.

The degree of wetting and apparent melting increases with decreasing $KAlO_2$ content of the pellets to the point where complete coalescence of the melt into corners of the foil occurs (Fig. 3-b). However, features indicative of a strong interfacial effect can be seen also in the 100/0 composition. For certain grains in this experiment, an oriented intergrowth of rod-like crystals within a medium of lower surface tension is suggested. These rods appear to emanate from a point and spread radially outward, terminating with rounded ends (Fig. 6-a). The presence of two phases in these intergrowths or at least of two crystallographic orientations with dramatically different surface tensions (Fig. 6-b) is suggested. Only certain of the K_2CO_3 grains show this structure. The amount of Pt in all of these grains, regardless of structure, is uniformly low (est. <1 wt%). In certain crystals the oriented structure is present only in the outer portions. The 100/0 experiments invariably yield a dark gray product, as opposed to the green color of the experiments which contain $KAlO_2$.

The results of the doubly encapsulated melting experiments (Fig. 1) are essentially in agreement with the results of the pellet experiments discussed above, although the former are not as amenable to SEM characterization, and so a comparison of the microstructures cannot be made at this time. However there is no indication of any platinum reaction or change in color in the sealed experiments. Thus, the anomalous melting behavior appears to be independent of platinum reaction or interaction with air.

High temperature x-ray data for the 80/20 composition under dry nitrogen show that the K_2CO_3 in these mixtures goes through at least two reversible subsolidus phase changes, and recrystallizes extensively near the reported melting point of 901 °C (ref. [6]) to give strong preferred orientation, thus making the actual determination of melting difficult. The principal aluminate (220) peak can be observed at all temperatures however and remains nearly constant in intensity. A phase change near 900 °C was observed visually through the port on the x-ray apparatus: a region of high thermal conductivity developed which upon further heating slowly spread throughout the pellet. This suggests but does not prove melting as recrystallization and densification could produce the same effect. Upon termination of high temperature x-ray experiments the samples showed no visual evidence of melting.

For all experiments x-ray patterns of the results taken at 25 °C show well-developed patterns of K_2CO_3 and $KAlO_2$. In this respect the patterns closely resemble those of appropriate mixtures of starting materials. Important exceptions are the powder vaporization series of experiments (Fig. 7). Extra lines occur in these patterns at 16.7°, 17.4°, 19.3° and ~29° values of 2θ (CuKα radiation). These extra lines do not occur in either pure K_2CO_3 or pure $KAlO_2$ subjected to similar heat treatment. Of these lines those at 17.4 and 19.3° correlate

reasonably well with those of a potassium platinate phase reported by ref. [9]. To a lesser degree this is true for the broad peak near 29°; however, the intensity of this peak is not in keeping with the potassium platinate pattern. Most importantly, it has not been possible to ascribe the first and strongest peak at 16.7° to any known phase. All four extra lines remain relatively constant in intensity until all of the K_2CO_3 has evaporated (Fig. 7-d) - then they vanish abruptly along with the coloration. Additionally, low angle lines have been detected for certain compositions in this series, corresponding to periodicities in the 50-100A range (Fig. 8). These are difficult to reproduce, they appear to be very sensitive to methods of preparation, and they vanish rapidly upon atmospheric exposure. Relatively high effective vapor pressure of "K_2O" or K_2CO_3 is thought to be essential. It should be noted that these low angle peaks have been detected only in $K_2CO_3/KAlO_2$ mixtures, and a considerable amount of time was spent in attempting to differentiate what are judged to be genuine specimen diffraction effects from machine-related artifacts. It is significant that lamellar features can be seen on fracture surfaces in SEM micrographs of these experiments (Fig. 9) which have dimensions approaching those indicated by the low angle patterns.

Any reasonable hypothesis for correlation of the data presented above must explain in particular the sudden change in apparent melting behavior with composition (e.g. between 90/10 and 92/08 at 1150 °C). Consequently, a phase change seems to be required. Two possibilities can be suggested: 1) formation of unquenchable solids at high temperature and 2) the existence of intermediate solid/liquid (mesomorphic) phases.

The occurrence of unquenchable high temperature solid solutions does not appear to be supported by high temperature x-ray data, although vaporization and recrystallization near the melting point make any such interpretation difficult. It is perhaps significant in this regard that Knudsen effusion measurements of K pressures over a 60/40 composition give values very close to those for pure K_2CO_3 at 900-1100 °C [10], indicating that any structural interaction with $KAlO_2$ must be relatively weak if it exists. An unusual type of structure would need to be proposed, most probably of a mixed layer or intercalation type. It can be said with certainty on the basis of the high temperature x-ray experiments that the room temperature monoclinic form of K_2CO_3 [11] is not stable above 500-600 °C, and that a transition to a hexagonal polymorph reported in the pure end member [12] occurs in mixtures as well. Given the existence of rapid reversible phase transitions in K_2CO_3, the extra lines on the room temperature powder patterns of Figures 7 and 8 must be viewed with caution, as they are likely to represent metastable structures.

The possibility of mesomorphic behavior is at present perhaps the strongest. While not a commonly observed high temperature phenomenon, it has been reported in certain inorganic systems [13]. Furthermore, pure K_2CO_3 exhibits unexplained behavior near its melting point. This is evidenced in the existence of anomalously high K pressures at the melting point [10] and the suggestion of high viscosity as melts are

cooled through the crystallization temperature. In addition to chemical similarity, the K_2CO_3 and $KAlO_2$ structures possess a number of features which would make such mutual intergrowth energetically possible, and perhaps favorable, both as ordered liquids at high temperature and as intercalated or epitaxially intergrown solids in the subsolidus region. The high temperature x-ray data suggest that the thermal expansivities of K_2CO_3 and $KAlO_2$ may be similar, making close association of the lattices along an interface reasonable, provided minor structural readjustments are possible. Such interfacial association of these compounds has been investigated by treating idealized lattices of K_2CO_3 (primitive hexagonal) and $KAlO_2$ (m3m) via the computer program MATCH 1 (ref. [14]). Results indicate that intergrowth along an interface defined by K_2CO_3 (001) and $KAlO_2$ (111) is both possible and likely. The former plane is preferred by the author over others in potassium carbonate, as this is the plane in which the carbonate ions are aligned. Figure 10 shows one way of superimposing the two lattices such that negligible cumulative mismatch results for distances of several hundred angstroms, largely eliminating the need for dislocations (potassium ions have been positioned by analogy with the Na_2CO_3 structure [15] and the ideal cristobalite structure [16]). A hexagonal symmetry is evident in the pattern of site coincidences. It is suggested that ordered interfacial intergrowths of this type [possibly along the (110) or (100) planes of $KAlO_2$] could be responsible for the unaccounted-for extra lines in Fig. 7. If an ordered or partially ordered planar arrangement is present in a mesophase at high temperatures, solidification might tend to preserve this arrangement insofar as structurally possible. Additional effects such as intercalation of Pt and K or ordering of vacancies might also occur, especially in association with a planar interface. This could account for the coloration and the low angle periodicities observed in the powder patterns.

2. K_2O-CaO-Al_2O_3-SiO_2

As an aid to experimental investigation, the development of models for calculation of MHD slag liquidus surfaces was continued. Following the approach outlined in the previous quarterly reports, ideal solution calculations were first performed to establish a basis for the calculation of excess functions eliminating the difference between ideally calculated and observed liquidii. Results of ideal solution calculations for several binary joins within the quaternary system are shown in Figures 11-13. These diagrams have been drawn using an iterative program developed by the author which first solves the following equations for convergence:

$$-\ln X_A^{melt} = -\ln X_A^{x\ell A} + \frac{\Delta H_A^{fusion}}{R}\left(\frac{1}{T} - \frac{1}{T_A^{fusion}}\right)$$

$$-\ln X_B^{melt} = -\ln X_B^{x\ell B} + \frac{\Delta H_B^{fusion}}{R}\left(\frac{1}{T} - \frac{1}{T_B^{fusion}}\right)$$

where X is mole fraction, A and B refer to end members, R is the gas constant, T the temperature kelvin and ΔH^{fusion} the enthalpy of melting. Following this the program plots liquidus curves and measured eutectic points as shown in the illustrations. Measured values are taken from previous reports and from ref. [17]. The agreement between calculated and observed is not good, reaffirming the marked non-ideality of these silicate solutions with respect to molecular end members. The sole exception appears to be $KAlSiO_4$-$KAlSi_2O_6$ (not shown); however, this may be in part fortuitous since the thermodynamic data were derived from the phase diagram [8].

An attempt will be made during subsequent quarters to develop the quasichemical melt polymerization model outlined in ref. [2] for detailed application to the system K_2O-CaO-Al_2O_3-SiO_2, in conjunction with continued experimental work. Also, it is hoped that soon a program recently written by the author for quasichemical calculation of multicomponent liquidus surfaces can be applied.

Plans: Extend K pressure measurements to additional compositions in the K_2O-CaO-Al_2O_3-SiO_2 system. Analyze existing data for model slags obtained thus far in an attempt to obtain unifying relationships between K pressure and composition.

Continue experimental work in K_2O-CaO-Al_2O_3-SiO_2. Develop program for calculation of liquidus surfaces according to quasichemical model.

References

1. E. R. Plante and L. P. Cook, Proc. 17th Symp. Eng. Aspects Magnetohydrodynamic Electrical Power Generation, Stanford, C.1.1. (1978).

2. L. P. Cook, 7th Int. Conf. on Magnetohydrodynamic Electrical Power Generation, Cambridge, Mass., V. 1, 212 (1980).

3. L. P. Cook, R. S. Roth, H. S. Parker, and T. Negas, Am. Mineral., 62 1180 (1977).

4. D. K. Smith, Norelco Reporter, 10 19 (1963).

5. A. Bon, C. Gleitzer, A. Courtois and J. Protas, C. R. Acad. Sci. Paris, 278C 785 (1974).

6. JANAF Thermochemical Tables, 2nd Ed., NSRDS-NBS 37, U.S. Dept. Commerce (1971).

7. R. S. Roth, Advances in Chemistry Series, Amer. Chem. Soc., Washington, D.C. (in press).

8. F. E. Spencer, J. C. Hendrie, Jr., and D. Bienstock, 6th Int. Conf. on Magnetohydrodynamic Electrical Power Generation, Washington, D.C., V. 2, 181 (1975).

9. C. L. McDaniel, Nat. Bur. Stand., pers. comm. (1980).

10. E. R. Plante, Nat. Bur. Stand., pers. comm. (1980).

11. P. M. deWolff, File No. 16-280, JCPDS Int. Centre for Diff. Data, Swarthmore, PA.

12. S. J. Schneider and E. M. Levin, J. Amer. Ceram. Soc., 56 218 (1973).

13. P. G. de Gennes, The Physics of Liquid Crystals, Oxford Univ. Press, London (1974).

14. B. Dickens and L. W. Schroeder, Nat. Bur. Stand. Tech. Note 893, 71 p. (1976).

15. G. C. Dubbeldam and P. M. deWolff, Acta. Cryst., B25 2665 (1969).

16. M. O'Keeffe and B. G. Hyde, Trans. Amer. Crystallog. Assoc., 115 65 (1979).

17. E. M. Levin, C. R. Robbins, and H. F. McMurdie, Phase Diagrams for Ceramists, Columbus, Ohio, The American Ceramic Society (1964).

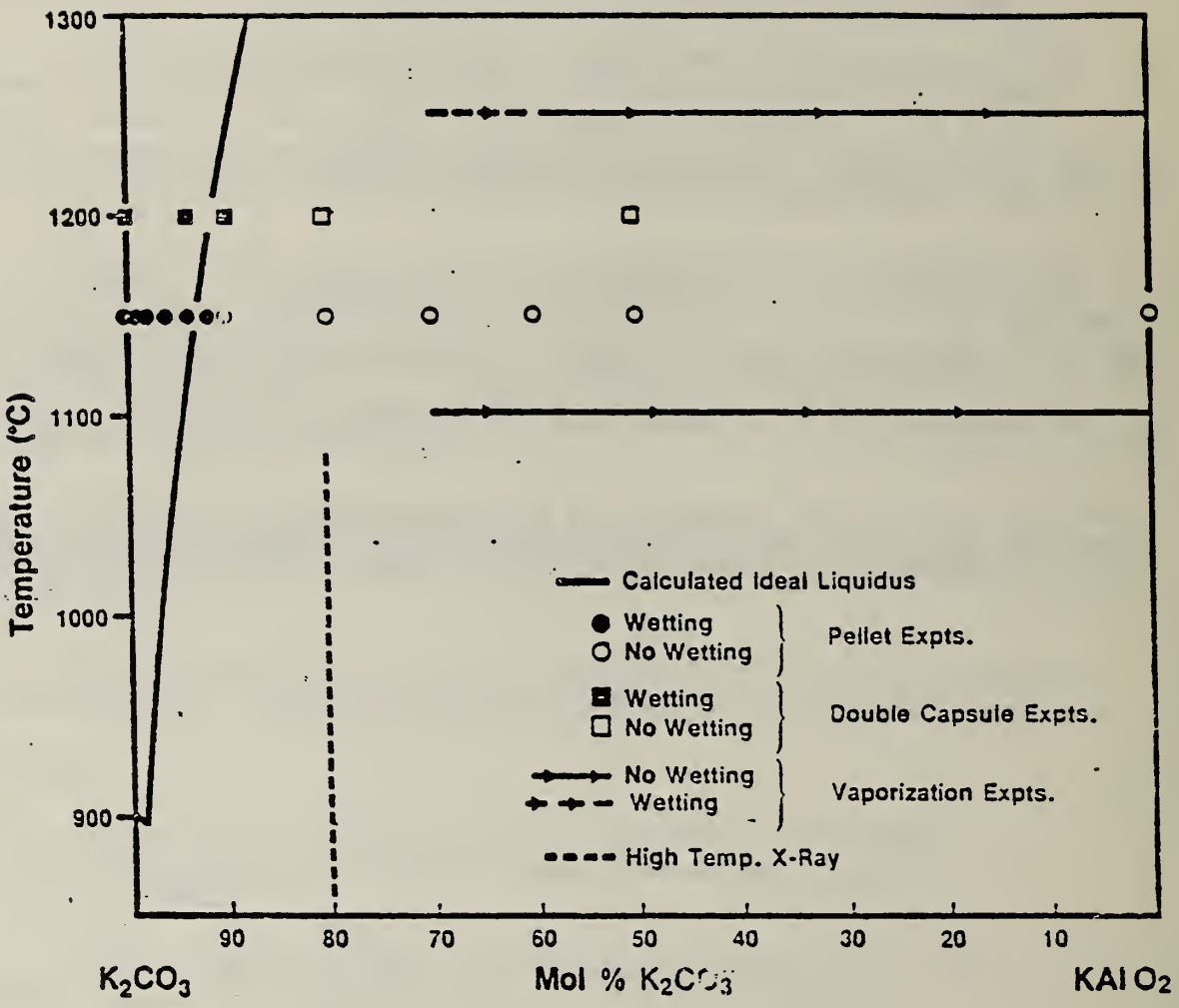

Fig. 1. Experimental data for K_2CO_3-$KAlO_2$, with calculated (ideal) liquidus for comparison.

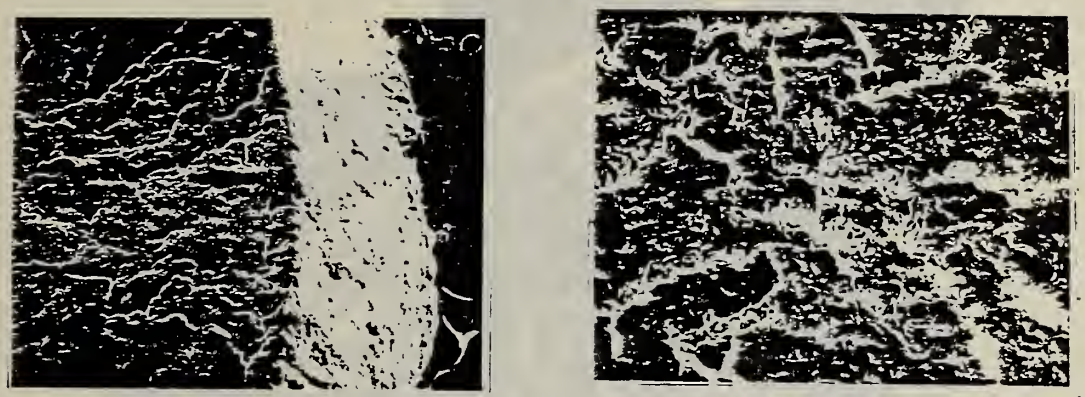

a b

Fig. 2. SEM micrographs of 90/10 pellet heated at 1150°C, 5 min. Bars represent 100 μm. Note sharp upper edge of pellet visible in Fig. 2-a, which suggests lack of melting. Fig. 2-b illustrates the development of coarse crystallinity on the surface.

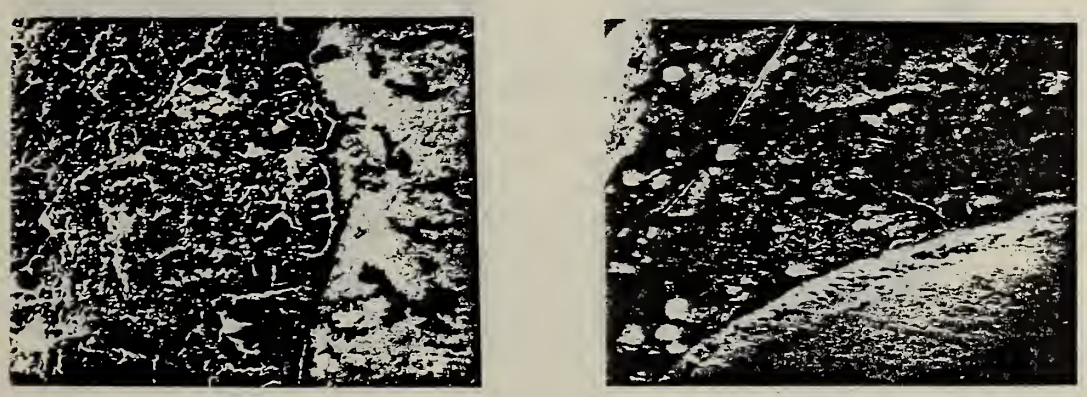

a b

Fig. 3. SEM micrographs of melted 92/08 (a) and 100/0 (b) pellets heated at 1150°C, 5 min. Bars represent 100 μm and 1 mm. Melt (dark areas on lighter Pt foil) has not coalesced into corners of foil in (a) as it has in (b).

Fig. 4. SEM mosaic of surface of melted 92/08 pellet, Fig. 3-a. Bar represents 10 μm.

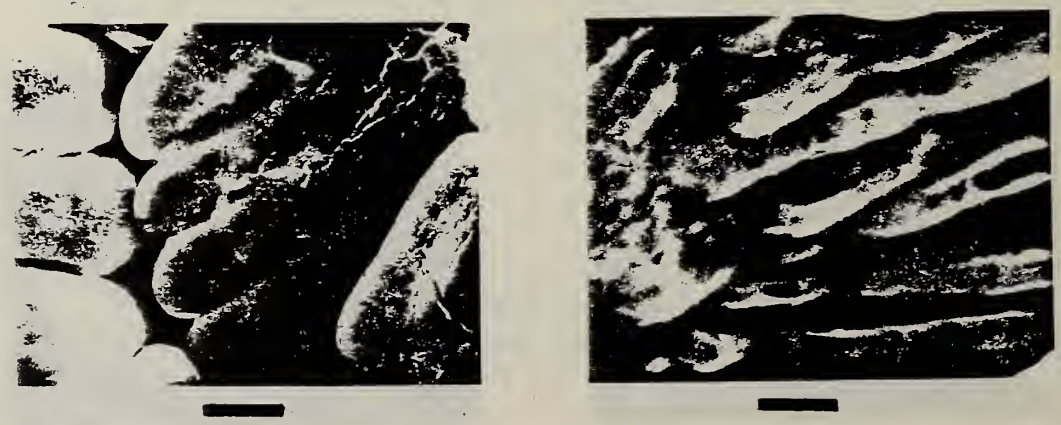

a b

Fig. 5. Surface of melted 92/08 pellet, Fig. 3-a. Bars represent 10 and 1 μm.

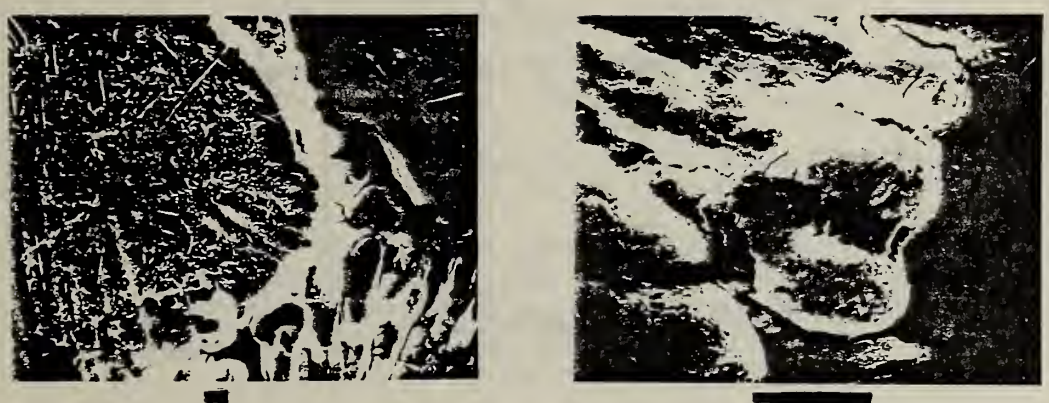

Fig. 6. Surface of melted 100/0 pellet, Fig. 3-b. Bars represent 10 μm.

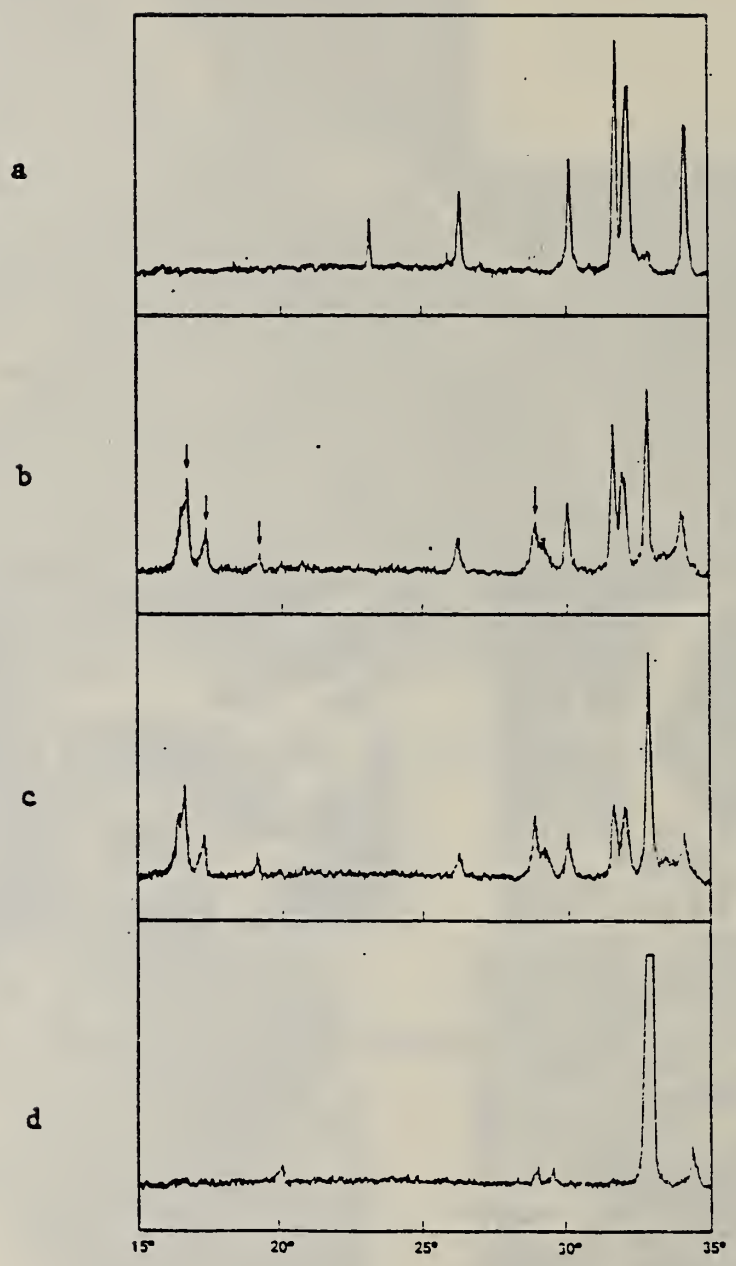

Fig. 7. X-ray powder patterns (2θ vs. intensity). Fig. 7-a is from pure K_2CO_3 starting material dried at 160°C under vacuum. Figs. 7-b,c,d are from vaporization experiments at 1250°C. Compositions determined by weight loss are as follows: b) 60/40, c) 10/90, d) 0/100. Arrows in b) show extra lines.

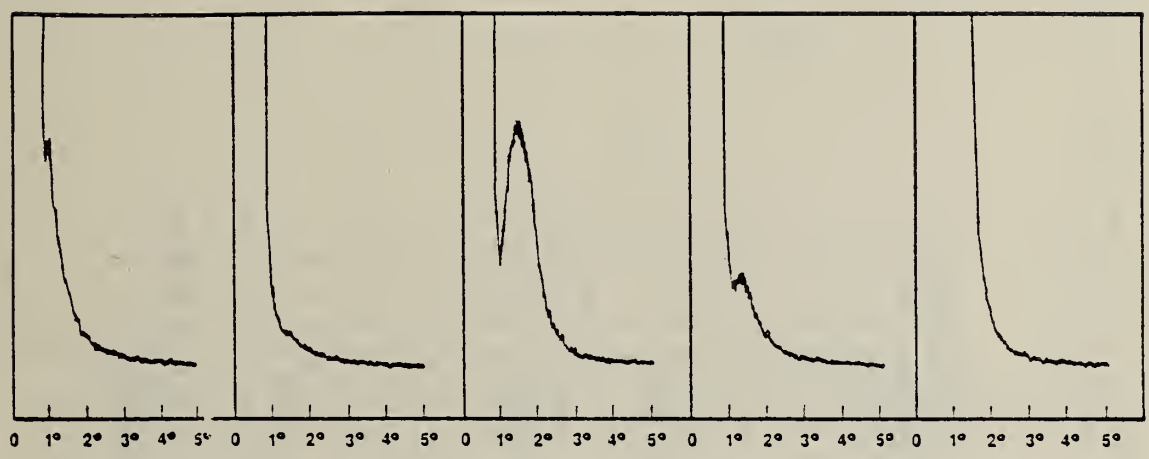

Fig. 8. Low angle portions of powder patterns (2θ vs. intensity) from 50/50 powder heated in the presence of excess K_2CO_3 at 1250°C. Beginning with the right, cumulative heat treatments are 30, 45, 60, 90 and 120 min.

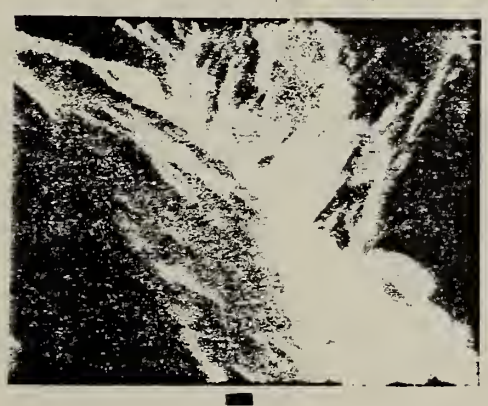

Fig. 9. SEM micrograph of fracture surface of vaporization experiment near 65/35. Note lamellar structure, upper right. Bar represents 100 nm.

Fig. 10. Matching of potassium sites in K_2CO_3 along hypothetical K_2CO_3 (001)/$KAlO_2$ (111) interface.

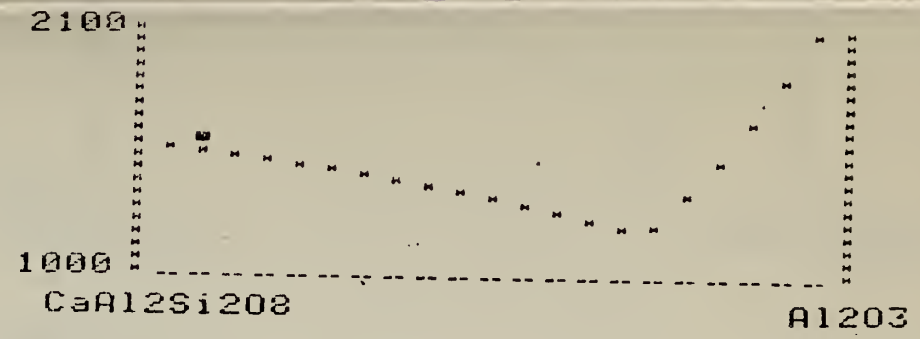

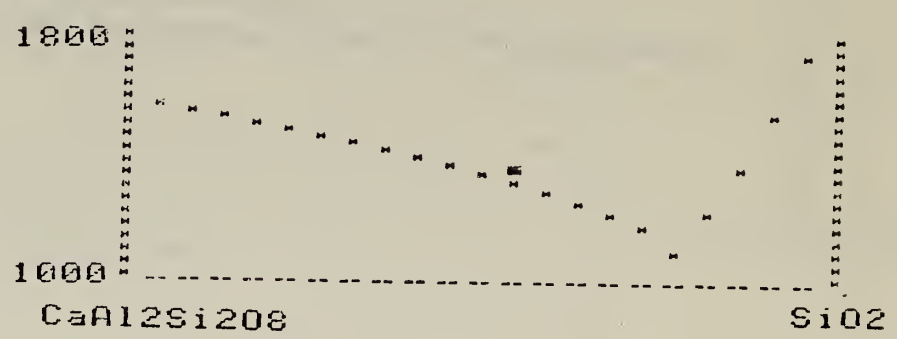

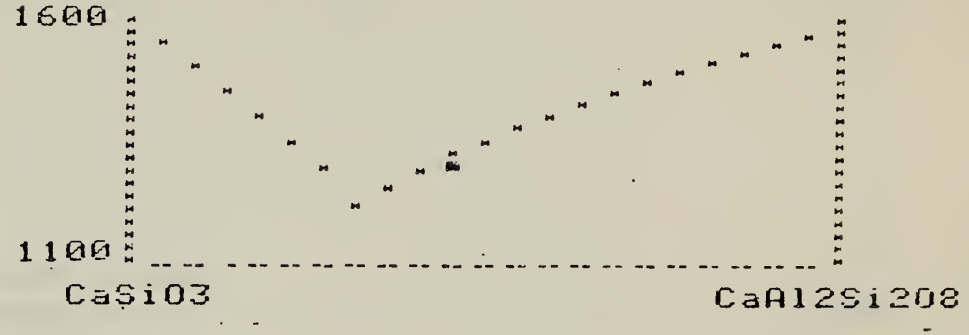

Fig. 11. Discrepancy between ideally calculated liquidus and measured eutectic (solid rectangle) for CaO-Al_2O_3-SiO_2 joins.

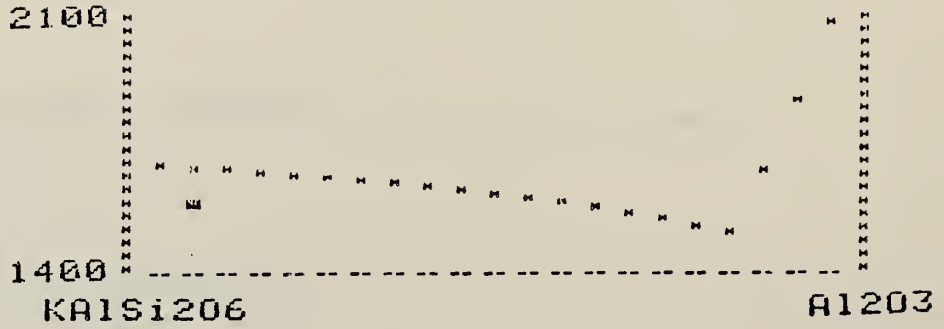

Fig. 12. Discrepancy between ideally calculated liquidus and measured eutectic (solid rectangle) for joins with leucite in quaternary system K_2O-CaO-Al_2O_3-SiO_2.

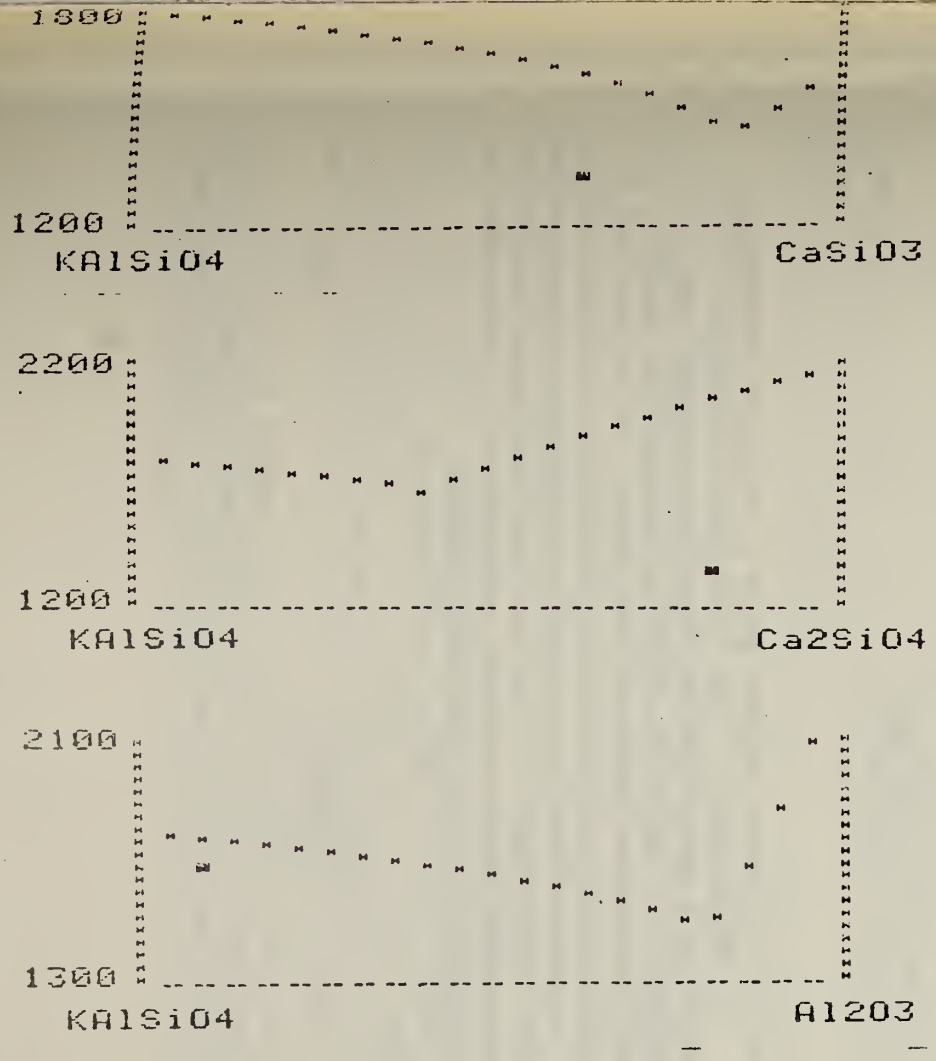

Fig. 13. Discrepancy between ideally calculated liquidus and measured eutectic (solid rectangle) for joins with $KAlSiO_4$ in quaternary system K_2O-CaO-Al_2O_3-SiO_2.

2. Electrical Conductivity and Polarization (W. R. Hosler)

Progress

Slag Electrical Conductivity

In the last quarterly report (April - June 1980), a detailed description of the sample preparation and measurement technique was presented. Figure 5 of the corresponding section of that report shows a radiograph of a typical slag sample with the leads attached and numbered. Figure 1 is a reproduction of that radiograph in this report for the convenience of the reader. The measurement technique and the data acquisition system have been extended to include the potential measurements between all probe sets, i.e. V_{12}, V_{23}, V_{34} and V_{14}. This has the advantage of being able to detect where polarization or abnormalities exist along the length of the sample with respect to the center of the sample. The center of the sample, monitored by probes 2 and 3, is the area where the bulk conductivity is measured and where it is assumed little or no polarization exists because no current is being drawn through the two contacts involved. This is because the potential between probes 2 and 3, as well as the other probe sets, is measured by a voltmeter whose input impedance is high compared to the sample resistance between those two probes. At the same time, current is introduced to the sample through probes 1 and 4, and it is at these areas where polarization and other effects may be observed. Consider the equation

$$f_{14}(V) = \frac{V_{12} + V_{23} + V_{34}}{V_{23}\, d_{14}/d_{23}} - 1 \qquad (1)$$

where d_{14} and d_{23} are the distances between probe 1 and 4 and between 2 and 3 respectively. The denominator of the first term in equation 1 is the potential between 1 and 4 normalized to the value between 2 and 3. This, of course, presumes that the cross-sectional area of the sample remains the same along the entire length of the sample. If it does not, these adjustments must be made in the normalization factor. If the value of equation 1 is zero or near zero, no polarization or inhomogeneities exist along the sample length except in the possible case that a deviation of V_{12} from the norm is equal to the negative deviation of V_{34} from the norm. This can be detected by use of the relationships:

$$f_{12}(V) = \frac{V_{12}}{V_{23} d_{12}/d_{23}} - 1 \qquad (2)$$

and

$$f_{34}(V) = \frac{V_{34}}{V_{23}d_{34}/d_{23}} - 1 \qquad (3)$$

which again represent the deviation from the norm of the potential value between probes 1 and 2 (equation 2) and between 3 and 4 (equation 3). If $f_{12}(V)$ and $f_{34}(V)$ are near zero, no polarization or inhomogeneities exist along the sample. If either or both of these values deviate widely from zero, polarization and/or inhomogeneities may exist. Figures 2 and 3 show plots of the values for equations 1, 2, and 3 for a slag sample measured with increasing temperature (Figure 2) and with decreasing temperature (Figure 3). These datawere taken using a constant DC current and with equilibrium established at every point. This equilibrium was established by monitoring the potential between probes 2 and 3 as a function of time. When this value changed over a period of 15 minutes by less than 1 percent, datum for the temperature point was taken.

It is apparent that there are substantial differences between the curves for increasing and for decreasing temperatures below 1300 °C. This will be discussed later. It should be noted, however, that at temperatures above 1300 °C both figures show a marked increase in the f(V) values (with the exception of $f_{12}(V)$) which indicates an increase in the polarization effects because of enhanced ionic conductivity. Electric fields along the sample were kept at approximately 1 volt/cm in order to avoid possible permanent polarization. A more dramatic increase in the f(V) values would be observed using higher electric fields.

This result is in agreement with the argument set forth in several previous quarterly reports that above 1385 °C the conductivity in this particular coal slag (derived from ash products of a Bow, NH steam generating plant) is predominantly ionic.

AC Conductivity Measurements (Four probe)

At each equilibrated temperature AC conductivity measurements were made along with the DC measurements described above. The data at each temperature pointwere taken as a function of frequency from 40Hz to 40KHz. This limitation of frequency was imposed because of the AC voltage sensing instrument's limited frequency response. The accuracy over this frequency range was 0.3 percent of the reading plus 0.04 percent of the 10V range used. For these AC measurements, however, a constant current was not used. The AC signal generator output voltage was adjusted to obtain nearly one volt on the conductivity probes for every temperature point. The current was measured as the potential drop across a standard (adjustable) resistor in series with the sample. The data scans were made in the same sequence as in the DC case described previously.

Figure 4 shows the data at 40Hz for f(V) values of the equations 1, 2, and 3 for increasing temperature, while Figure 5 gives the data for decreasing temperature. Since this was the same sample as the DC case and measured at the same time, the sample conditions should be the same.

Below 1300 °C, the corresponding AC and DC curves are similar. Since this is the case, it seems likely that the deviations from the near zero values expected for an ideal sample with no polarization, cracks, or inhomogeneities are caused primarily by inhomogeneities or microcracks. Polarization effects would not show up in the AC data at 40Hz, but would be apparent in DC data if ionic conductivity was prevalent.

On the other hand, there is a decided difference in the data for increasing temperature compared to those for decreasing temperature and this difference is evident for both DC and AC measurements. The reason for these differences may be attributed to the difference in sample treatment. The relatively rapid cooling of the sample from 1500 °C after the final filling process before contacts were applied probably results in some microcracks as well as some variation in crystalline components along the sample lengths. These effects show up in the f(V) data of Figures 2 and 4 differently than the f(V) data of Figures 3 and 5 for which the sample was cooled very slowly from high temperatures where microcracking should be minimized. It is interesting to note that $f_{34}(V)$ is negative and nearly constant in Figure 5 over the entire temperature range below 1300 °C while $f_{12}(V)$ is positive and monotonically increasing as the temperature decreases. This indicates that the condition of the sample in the volume between probes 3 and 4 is not changing appreciably as the sample is cooled, but in that volume between probes 1 and 2 it is changing. Under this situation, an analysis of the two ranges under a scanning electron microscope might reveal the nature of the different behaviors. This also demonstrates a case where a negative $f_{34}(V)$ partially compensates for a positive $f_{12}(V)$ and gives a $f_{14}(V)$ value nearer zero than it should be. The conclusion is that, since the AC and DC data are in relatively close agreement, polarization effects do not play a large role in the measurements and the conductivity in this temperature range is not predominantly ionic in nature.

Figure 6 is a plot of the conductivity as a function of frequency for the data taken with increasing temperature points while Figure 7 is for the same experiment taken with decreasing temperature. The increase in conductivity with increasing frequency at lower temperature in each case may be due to the capacity of the twisted lead pair from the sample to the data acquisition system. A rough calculation of this capacity leads to an impedance value at 40KHz of the same order of magnitude as the resistance observed between the conductivity probes. A room temperature measurement of the capacitative reactance of the lead pairs has confirmed this calculation.

At temperatures above 1300 °C, the 40Hz AC data shown in Figures 4 and 5 remain near zero in contrast to that data for the DC case (Figures 2 and 3). Polarization effects are not observed at 40Hz or over the frequency range measured and as a result, the f(V) values remain near zero.

Figure 8 shows the AC (40Hz) and DC conductivity taken with increasing temperature. The maximum at about 1100 °C and the minimum at 1150 °C are distinct although the AC and DC values at the minimum differ by nearly a factor of two. However, they are in near exact agreement above 1385 °C

where ionic conductivity is predominant and nearly equal below 100 °C where the slag is solid and electronic conductivity is probably predominant.

Figure 9 shows the AC (40Hz) and DC conductivity as a function of decreasing temperature. In this case, there is only an inflection point near 1150 °C and the AC and DC values differ again by about a factor of two. Since for both the increasing and decreasing temperature curves (Figure 9 and 9) careful attention was paid to obtaining equilibrated values, the reason for the difference in the curve shapes with increasing and decreasing temperatures is not clear. This should be investigated by SEM methods in an effort to determine the sample conditions under the two different situations.

It should be pointed out that previous electrical conductivity measurements on coal slag reported in previous quarterly reports were done by quenching the sample from some temperature above the softening point to a temperature (900 °C) below the softening point in order to quench in an established Fe^{+2}/Fe^{+3} ratio at lower temperature. These measurements were taken under equilibrated conditions so that the Fe^{+2}/Fe^{+3} ratio could change, depending on the temperature, at least above 900 °C.

From the results described above, obtained by the methods of measurement and sample preparation described previously, it is possible to arrive at certain conclusions about sample conditions during the course of the measurement. These conclusions are stated in the text. The main result is that these measurements support the viewpoint stated previously: that the electrical conductivity of slag from coal burned at the Bow, NH plant is predominantly ionic above 1385 °C. In addition, these measurements demonstrate that four-probe DC measurements are valid for obtaining a bulk conductivity of ionic conductors under certain conditions.

Plans: The electrical conductivity measurements reported over the last year have been for slags containing relatively large amounts of iron. These measurements will be extended to those slags containing less iron and more calcium which is typical of slags from Western coals. SEM investigations will be started in an effort to understand some of the anomalies described in the text of this report.

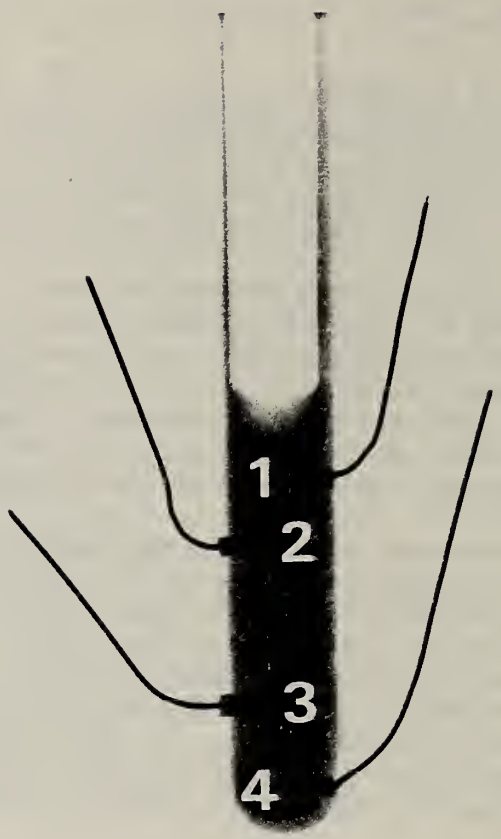

Figure 1. Radiograph of a typical slag sample. Platinum probes 1, 2, 3, and 4 are shown with probes 2 and 3 being the conductivity pair; and probes 1 and 4, the pair where current is introduced to the sample.

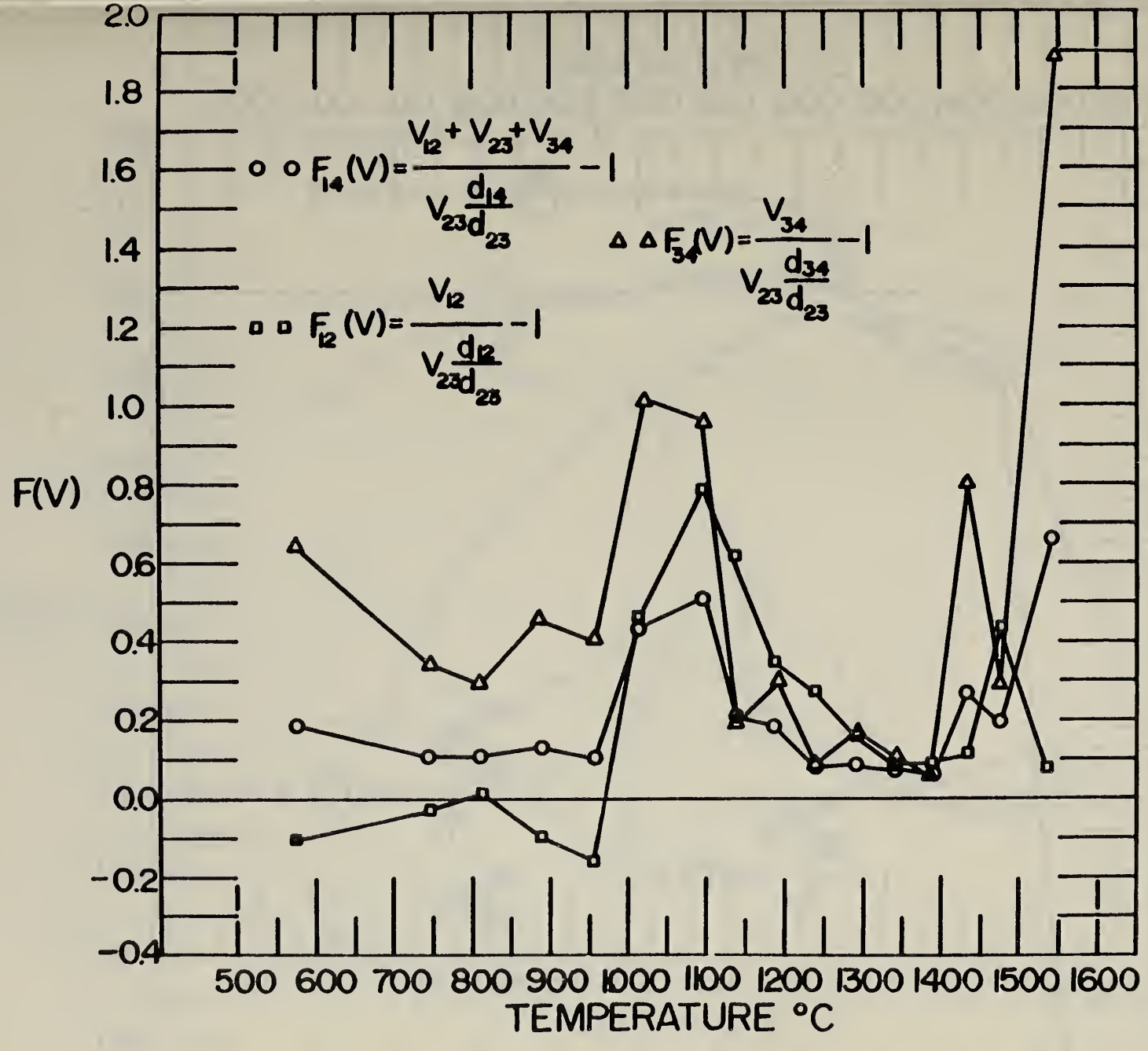

Figure 2. Plot of the DC values for equations 1, 2, and 3 as a function of temperature for increasing temperature.

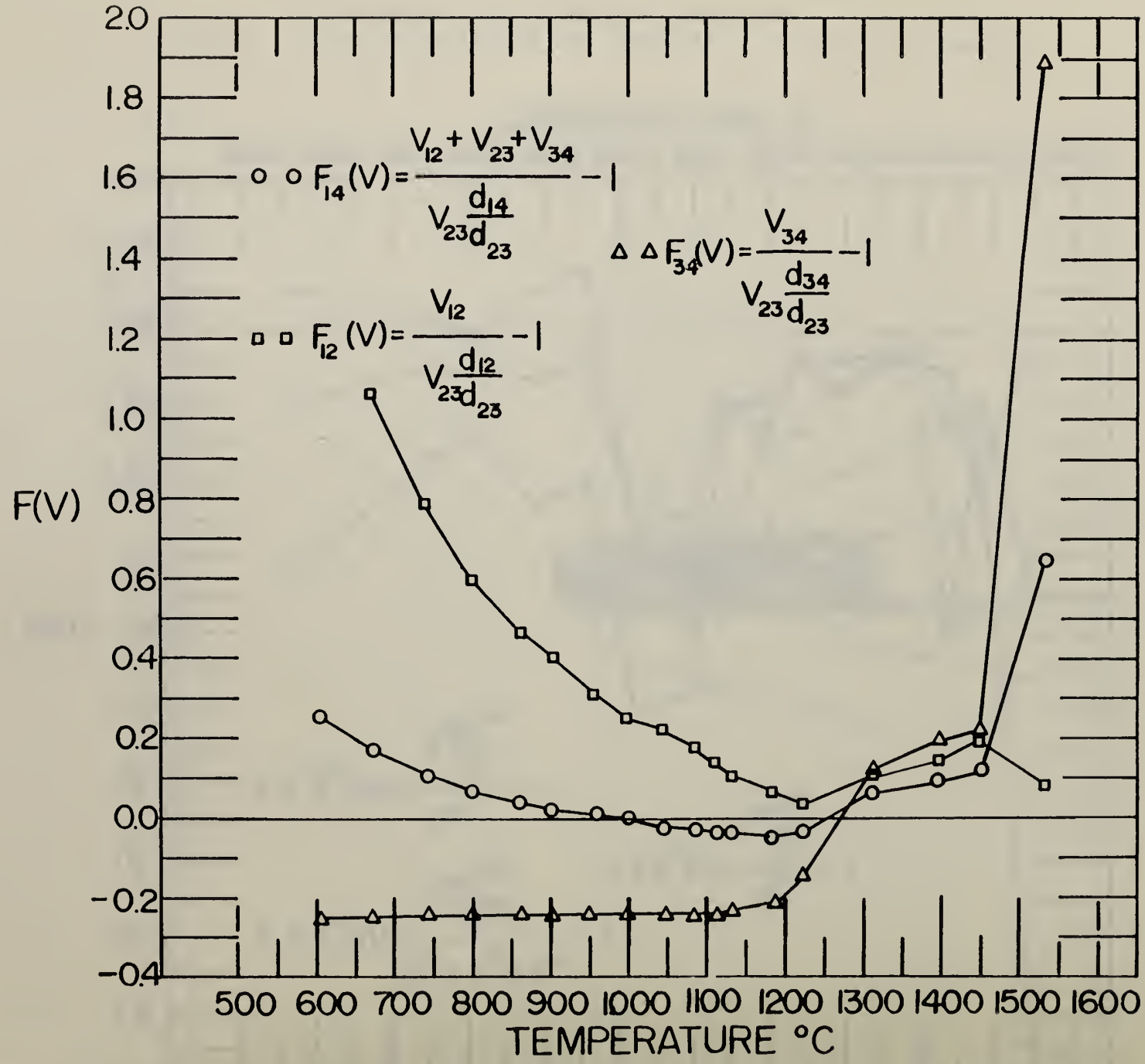

...ations 1, 2, and 3 as a function

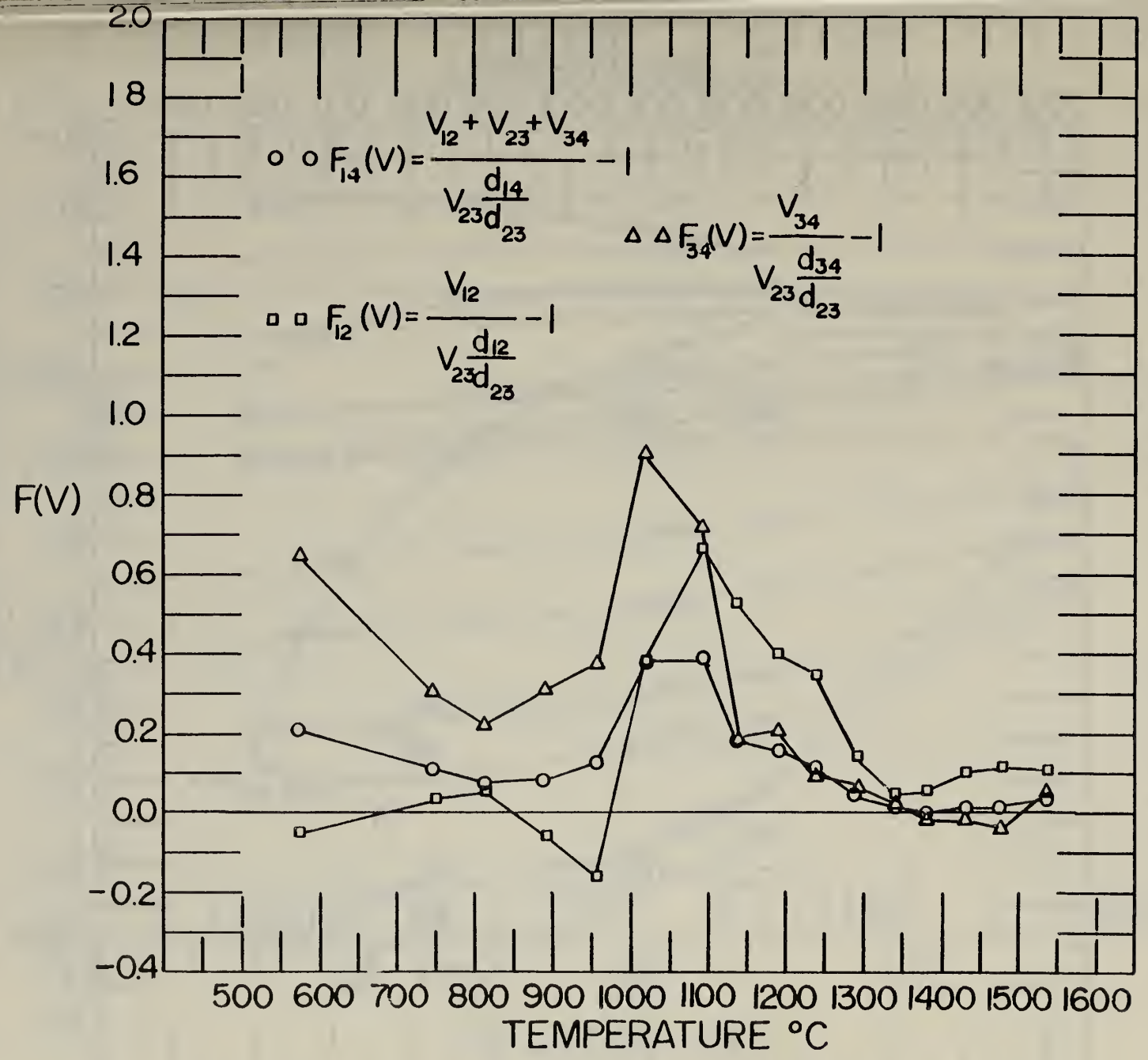

Figure 4. Plot of 40Hz AC values for equations 1, 2, and 3 as a function of temperature for increasing temperature.

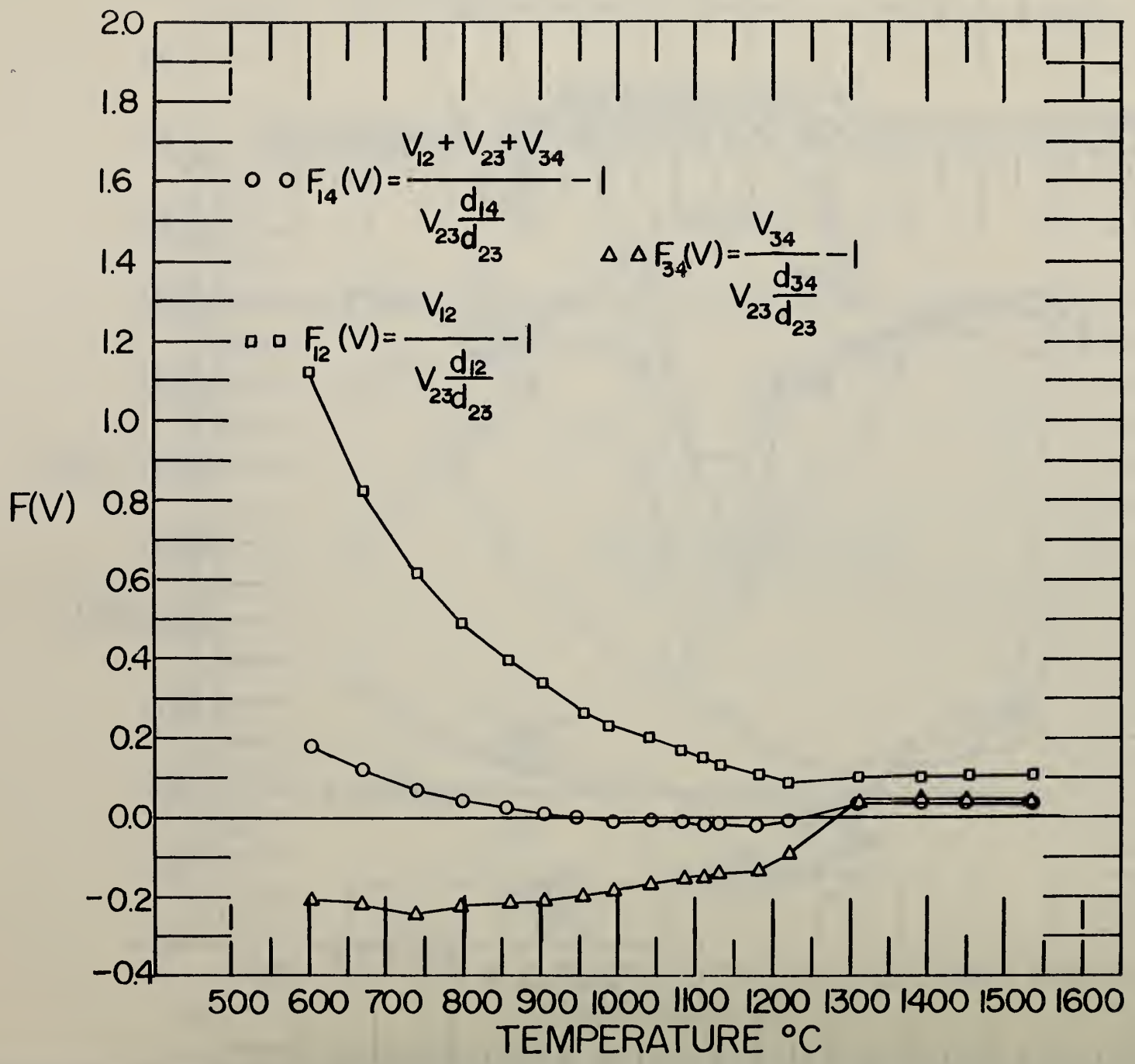
2.0
1.8
1.6
1.4
1.2
1.0
0.8
0.6
0.4
0.2
0.0
-0.2
-0.4
F(V)
o o $F_{14}(V) = \frac{V_{12}+V_{23}+V_{34}}{V_{23}\frac{d_{14}}{d_{23}}} - 1$
□ □ $F_{12}(V) = \frac{V_{12}}{V_{23}\frac{d_{12}}{d_{23}}} - 1$
Δ Δ $F_{34}(V) = \frac{V_{34}}{V_{23}\frac{d_{34}}{d_{23}}} - 1$
500 600 700 800 900 1000 1100 1200 1300 1400 1500 1600
TEMPERATURE °C

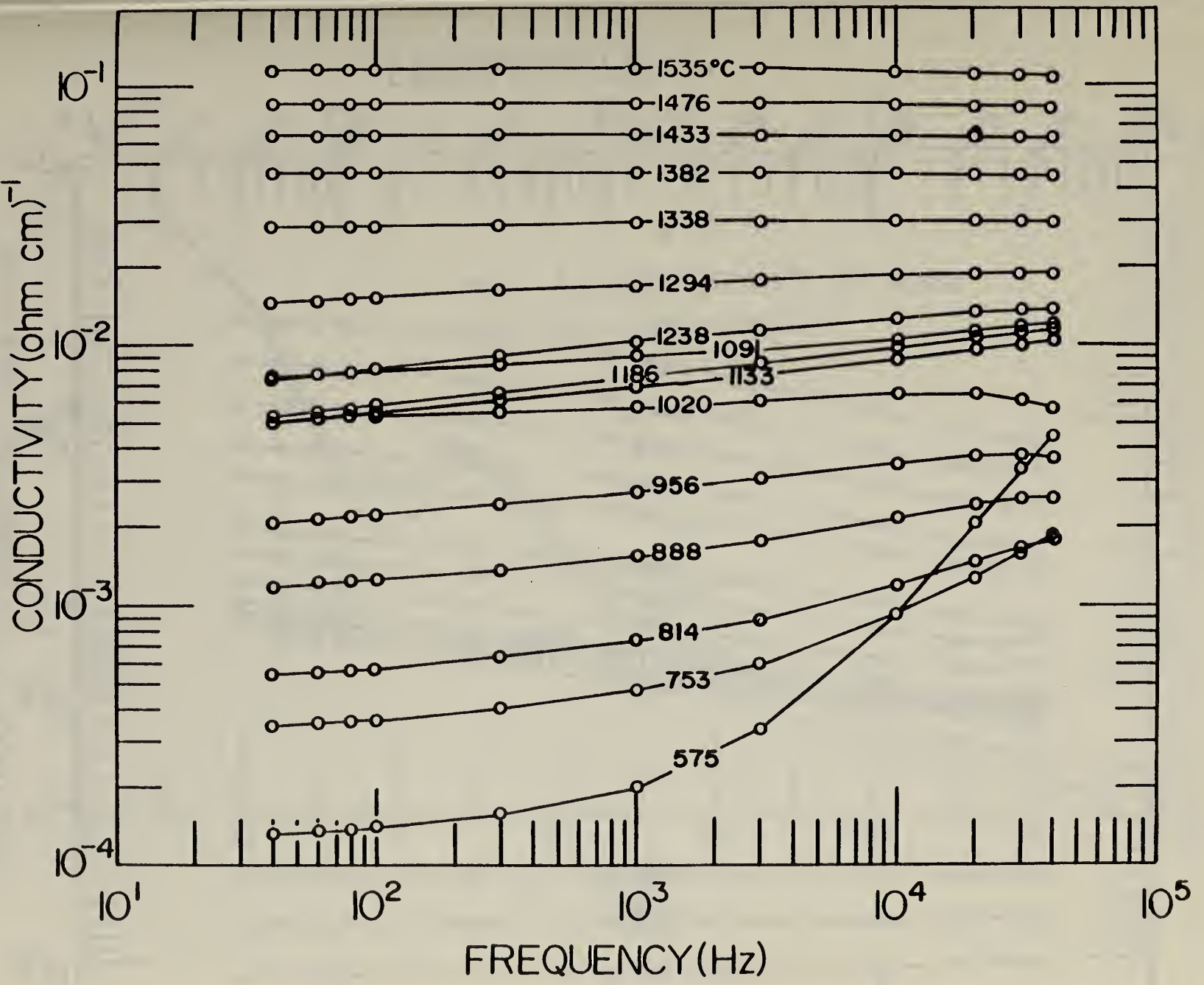

Figure 6. Conductivity as a function of frequency over a range of increasing temperatures.

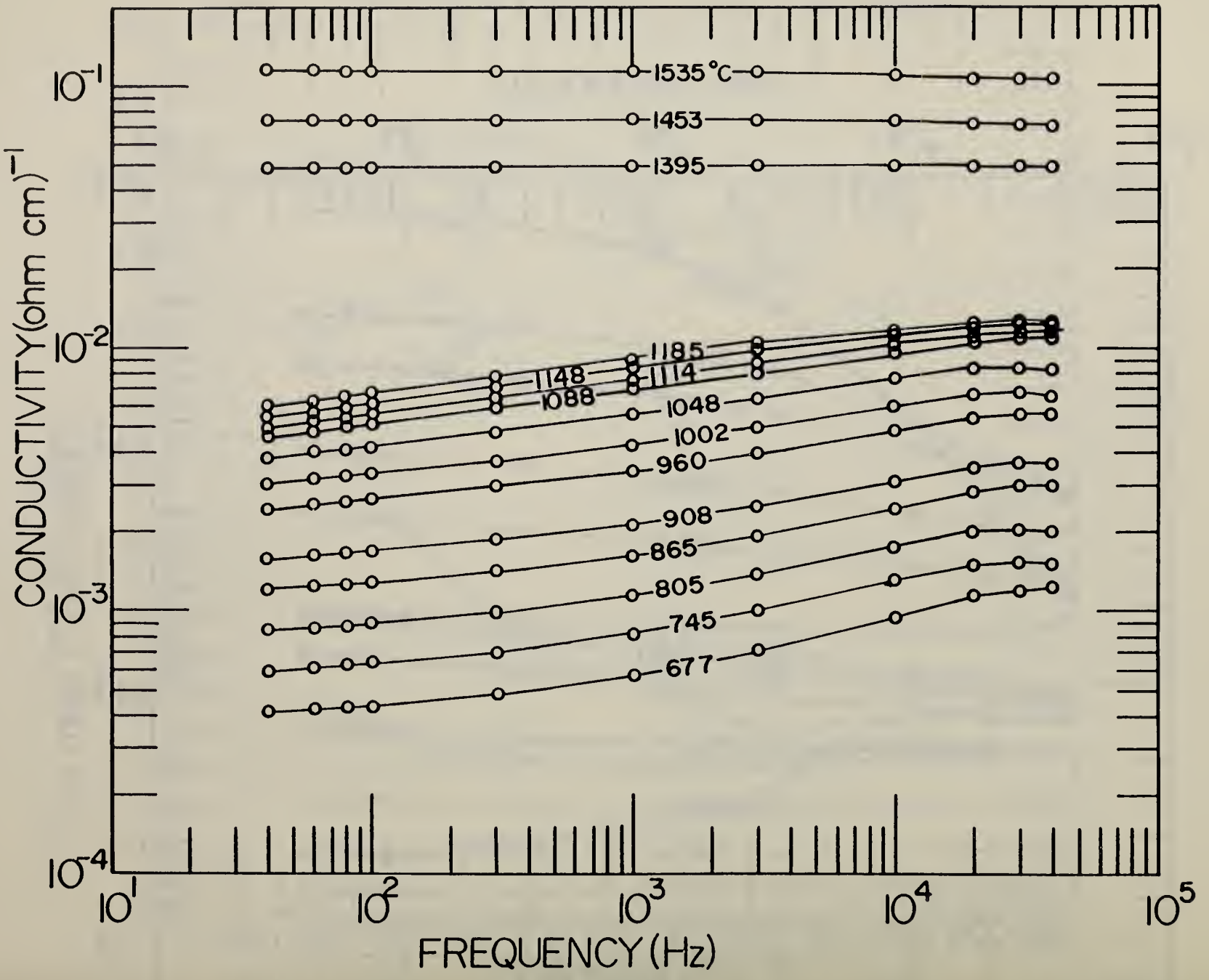

Figure 7. Conductivity as a function of frequency over a range of decreasing temperatures.

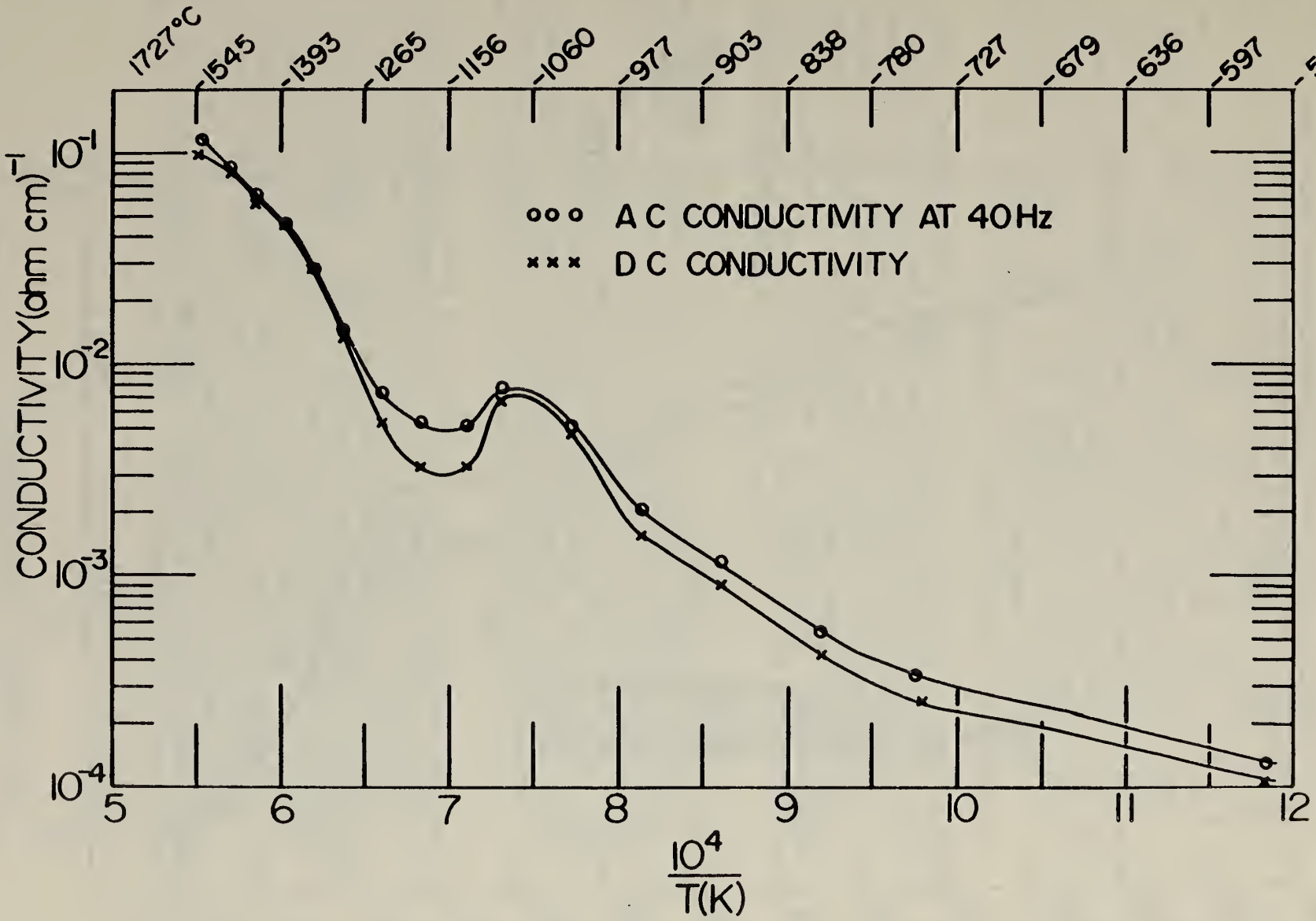

Figure 8. DC and 40Hz AC conductivity as a function of increasing temperature after sample preparation.

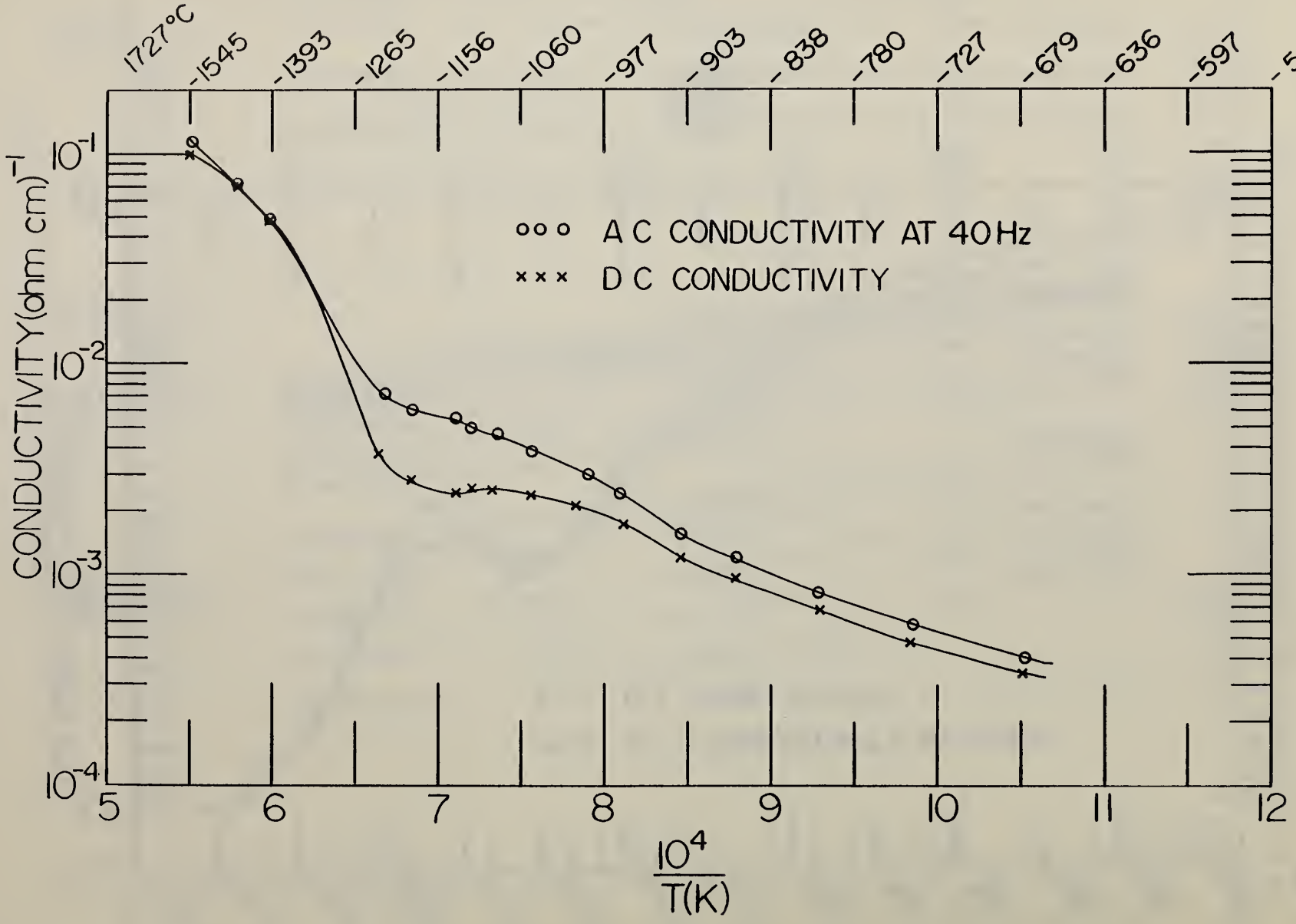

Figure 9. DC and 40Hz conductivity as a function of decreasing temperature from above 1500°C.

3. Corrosion of Downstream MHD Components (J. Smit and C. D. Olson)

Progress: Exposures of tubular specimens, Type 316 stainless steel, were performed under varied conditions of K_2SO_4, K_2SO_4-K_2CO_3 seed and oxygen rich or propane rich hot gas streams. All samples were exposed, exclusive of apparatus warm up and cool down, for a period of approximately four hours with seeding of 250 g of salt occurring in the first 25 minutes. Four stainless steel specimens were exposed under these general conditions, three at 590 °C and one at 500 °C. The sample temperatures were maintained using air to internally cool the tubular walls and the wall temperature was monitored using Pt/Pt-10%Rh thermocouple welded into the wall at the mid-length point. The gas stream temperature, in all cases, was held at approximately 1300 °C as indicated by a Pt/Pt-10%Rh thermocouple placed in the vicinity of the test specimen. The test specimens, following the exposure runs, were analyzed using SEM/EDX.

SEM/EDX Analysis of the Metal-Salt Deposit Interface - Test specimens were removed from the test rig upon cool down to approximately 40 °C and encapsulated immediately in epoxy to prevent any possibility of contamination and to reduce the possibility of hydration occurring in the salt coatings. Metallographic specimens were selected from the tubular specimen, 10 mm from the mid-length point. The specimens were cut, ground, and polished using non-aqueous media and stored in evacuated desiccators prior to SEM/EDX analysis.

Test specimens numbers 8-6, 9-6, and 6-6 were exposed at 590 °C and number 5-6 was exposed at 500 °C. All specimens exhibited similar salt deposit characteristics. The surface facing the gas stream was thinner than the deposit on the side portion of the tube (drip zone), and a thin fume deposit was found on the underside of the tube. The thickness of the top surface deposit was found to be consistent with previous samples in that, the surface salt deposit is thinner as the wall temperature increases. Also, under fuel rich conditions the deposit is thinner than in the oxygen rich environment.

An evaluation of specimens 8-6 (Figure 1) and 9-6 (Figure 24) can be made simultaneously. Both samples were seeded with 80% by weight K_2CO_3 and 20% by weight K_2SO_4, with wall temperatures of 590 °C, however, 8-6 was in an oxygen rich fuel environment and 9-6 was in a fuel rich environment. The variations in the salt deposit can readily be observed with the oxygen rich specimen (8-6) exhibiting a top deposit of 0.3 mm, drip deposit of 2 mm and a slight fume deposit. The fuel rich specimen (9-6) shows a top coating of 0.1 mm, drip deposit of 1.6 mm and a very unusual fume deposit region, dendritic in nature. Photos (Figures 2 and 3) show a banding property in the deposit with K + S near the surface of the steel followed by a high K region with a thin band of K + S on the surface. This phenomena is also seen in the

fuel rich specimen coating. The bulk of both coatings, however, is generally high in potassium (K) with moderate to low amounts of sulfur (S) found.

The corrosion process exhibited in both specimens seem to follow the same general corrosion mechanism. In sample 8-6 (oxygen rich) at the leading edge, salt-stainless interface (Figures 1, 4-12) we find the bulk stainless followed by a reaction zone area where high nickel is found with chromium and iron followed by an area of high chromium, high iron, nickel and potassium. Chromium and iron are then found penetrating the salt deposit with the iron being the most mobile species and moving far into the salt deposit. Nickel being the least mobil or least reactive species is generally not found to penetrate the salt deposit except at the interface where chromium and iron move rather readily through the salt.

In 8-6 (Figure 13), the corrosion or reaction zone can be seen at the drip zone salt deposit stainless steel interface region. This darker band region, as analyzed using EDX, Figures 13-20, shows high chromium, iron, low nickel, and potassium, indicating a reacted area on the metal surface. Analysis above and below this region again shows cation mobility. We find concentrations of the cations as follows: a) bulk stainless steel, b) higher nickel-chromium-iron, c) higher chromium-iron-nickel-potassium, d) chromium-high iron-potassium, e) iron-potassium, f) high potassium. Traces of sulfur are found in the coating and reaction areas, also, indicating some sulfur-cation reaction. Therefore, the SEM/EDX analysis seems to indicate a preferential leaching of the metal cations from the bulk materials (Type 316 stainless steel) in a somewhat orderly fashion as in the case of the 304 stainless steel. This can be corroborated by wastage (weight loss) experiments described in previous reports. The chromium and iron cations appear to be the more reactive species in the stainless steel and are preferentially leached by the potassium-sulfur salt. As these cations migrate from the bulk stainless steel composition to the salt deposit the relatively non-reactive nickel is left and what appears as layering is observed.

Figures 21-23 shows a portion of the fume deposit region where the corrosive process appears to be evident. On the edge, areas of low nickel are found, while areas of chromium, iron, potassium, and sulfur are found in the reaction zone. However, in the fume deposit region there is not as great a separation of the cations, as found by EDX, possibly due to the fact that no direct contact of the salt is made in this area during deposit but rather collected on the underside by vaporization.

In sample 9-6, fuel rich, at the leading edge of the stainless steel (Figures 24-34) we again find the bulk stainless steel followed by a reaction zone area. As in the fuel rich sample (8-6), what appears to be a distinctive corrosion banding appears using EDX analysis. The corrosive process in the oxygen rich fuel environment

appears to follow the same general pattern as found in the fuel rich environment. The cations are found again in a general order of mobility where: a) bulk stainless steel, b) higher nickel-high chromium-iron, c) chromium-iron-nickel-potassium, d) chromium-higher-iron-potassium e) iron-potassium, f) high potassium. Again sulfur is found in small amounts in the reaction zone area and coating.

In the fuel rich environment the reaction zone area does not appear to be as distinct as in the oxygen rich environment. The fuel rich system shows no areas of high nickel above the bulk stainless steel but shows high nickel associated with high chromium. There is, in general, more sulfur present when higher nickel is found, possibly forming nickel-sulfur compounds. As shown previously in the oxygen rich environment, the fuel rich environment shows that chromium and iron are the most mobile cation species that penetrate the salt deposit.

The drip zone region also exhibits a reaction band area in the fuel rich system. The same corrosion process is observed in this area as previously describe for the top of the tube. The fume deposit region examined exhibits a reaction zone area while the salt deposit shows high potassium content. Again iron and some chromium is found in the fume deposit, indicating the relative ease for these cations to migrate.

In sample 6-6, the tube wall was maintained at 590 °C but the corrosive salt used was K_2SO_4 in a fuel rich environment. As found in previous fuel rich systems the coating was thin on the leading edge of the tube, 0.1 mm, while the drip zone region built up, 1 mm. The fume deposit exhibited an unusual formation of material build up similar to what was observed in 9-6. The coating appears to have a more columnar nature which has been observed with previous samples using K_2SO_4 salt exclusively.

The reaction zone area in 6-6 (Figures 35-43) is not well delineated in the fuel rich system as compared to the oxygen rich system, however, corrosion is observed. SEM/EDX analysis indicated that the reaction bands above the stainless steel bulk composition have the following sequence: a) low chromium-nickel-iron, b) high chromium-iron-no nickel, c) chromium-iron-potassium, d) high potassium-chromium-iron, e) high potassium-iron, f) high potassium. Traces of sulfur are associated with the potassium but the bulk of the salt coating is high in potassium. As found in previous specimens, nickel is absent in high concentration. At the interface no nickel is detected whether this be through loss of the nickel or its displacement to other areas not readily detectable is not apparent. However, the migration of chromium to the edge of the stainless steel is seen with iron and chromium penetrating the salt deposits. Examination of the drip deposit region show similar results as previously discussed with the absence or near absence of nickel at the metals edge, and with chromium and iron moving into the salt layer region. The fume deposit region showed minimal corrosion while the coating contained high potassium.

At a lower temperature 500 °C, corrosion is still observed in Type 316 stainless steel, 5-6, using K_2SO_4 salt in a fuel rich environment. Figures 44-49 shows the reaction zone area at the metal-salt interface at the leading edge. In this area we find, using SEM/EDX: a) bulk stainless steel, b) low nickel-high chromium-iron-potassium-sulfur, c) potassium-iron-chromium-sulfur, d) potassium-iron-sulfur, 3) potassium-sulfur. An area of high nickel is not detected while areas of high chromium and iron are readily decernable in the reaction zone. This corrosion mechanism is also found in the drip zone area and the fume deposit region, though both to a lesser degree.

Conclusion: The variances between fuel rich and oxygen rich environments in the presence of K_2SO_4 and K_2CO_3 are minimal. Corrosion of the Type 316 stainless steel seems to occur readily in both instances. The oxygen rich system, however, does seem to exhibit a more definable corrosion band area than the fuel rich system. Both systems show that iron and chromium are the more mobile species and that nickel is relatively unreacted. In the oxygen rich system the nickel can be followed from the bulk composition to the interface due to the migration of iron and chromium upwards from the bulk to the surface and then into the coating. In the fuel rich system nickel does not seem to be left behind or found in high concentrations even though iron and chromium are found to migrate into the salt deposit. In previous samples, nickel was found infrequently, but localized, in high concentrations in the high chromium region.

In general, therefore, both systems indicate the same metal cation movement from the bulk stainless steel into the salt deposit.

Plans: 1) Continue the study of Type 316 stainless steel using SEM/EDX analyses, 2) analyze collected x-ray diffraction data of residue salt deposit materials from fuel rich and oxygen rich system, and 3) examine the feasibility of using ceramic and metal coating on mild steels with testing of specific materials at 590 °C.

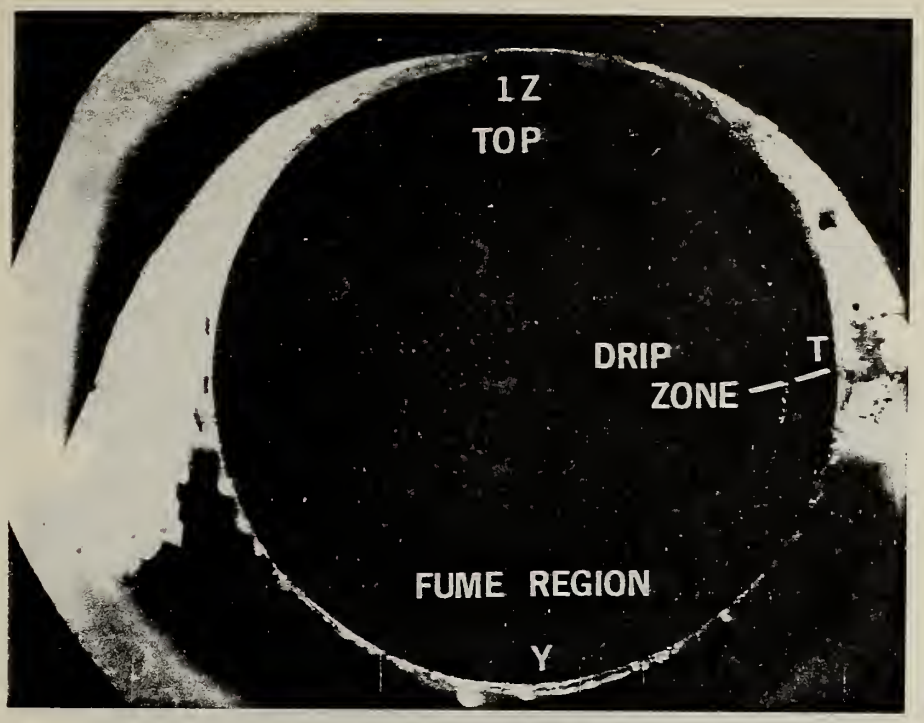

Fig. 1. Optical micrograph of a section of Type 316 stainless steel tubing after exposure to an oxygen rich hot gas stream seeded with K_2SO_4 and K_2CO_3. Tube temperature 590°C. Note deposit on upper surface of tube.

Fig. 2. SEM micrograph, 45 X, of region T of optical micrograph Fig. 1 showing metal-salt deposit interface in the drip zone.

Fig. 3. SEM micrograph, 92 X, of region T of optical micrograph Fig. 1 showing metal-salt deposit interface in the drip zone.

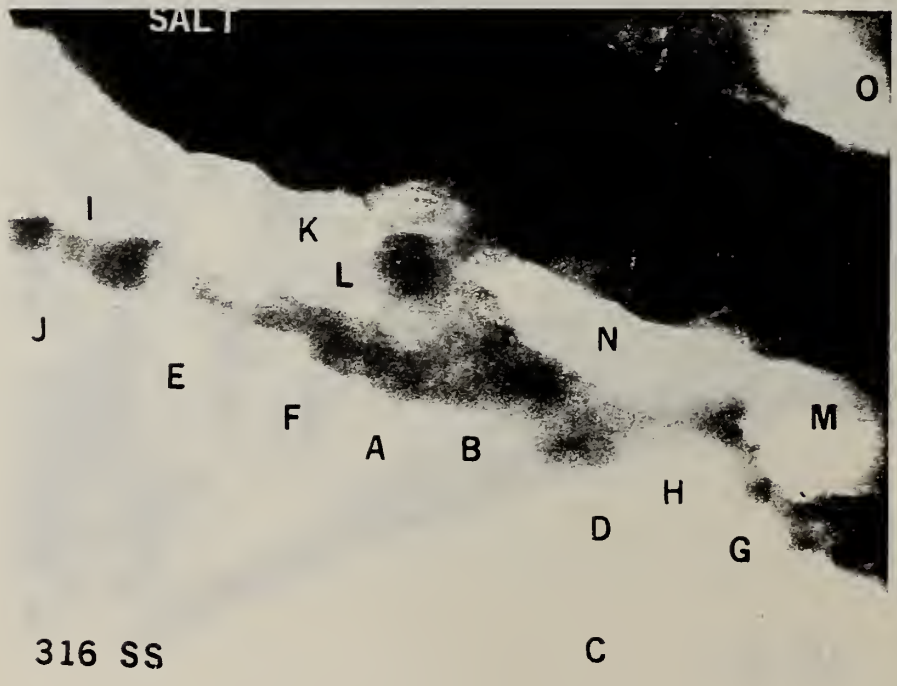

Fig. 4. SEM micrograph, 5460 X, of region 1Z of optical micrograph Fig. 1 showing reaction area at metal-salt interface. Lettered regions correspond to labeled EDX spectra Fig. 5-12.

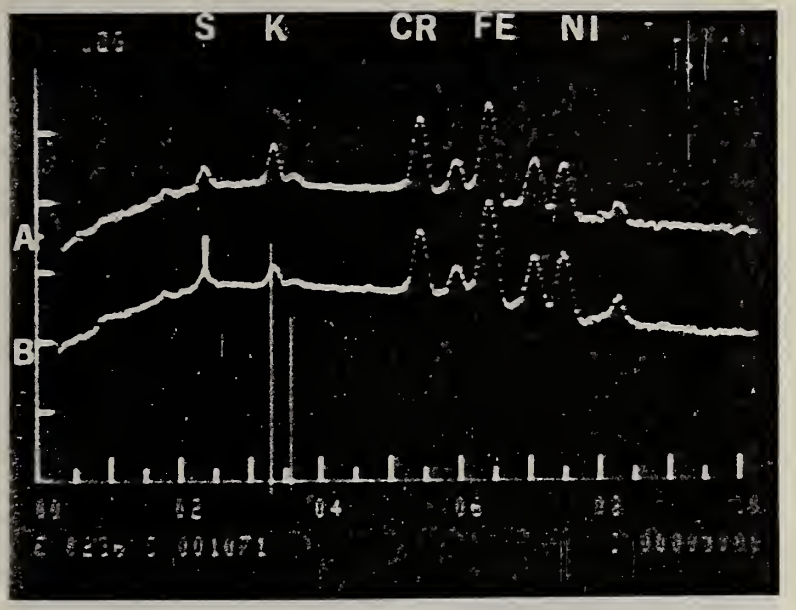

Fig. 5. EDX spectra of regions A and B of Fig. 4 showing slight increase in Ni concentration at metal-reaction zone interface (spectrum B). Specie position and designations of all spectra in this section of the report are as indicated above.

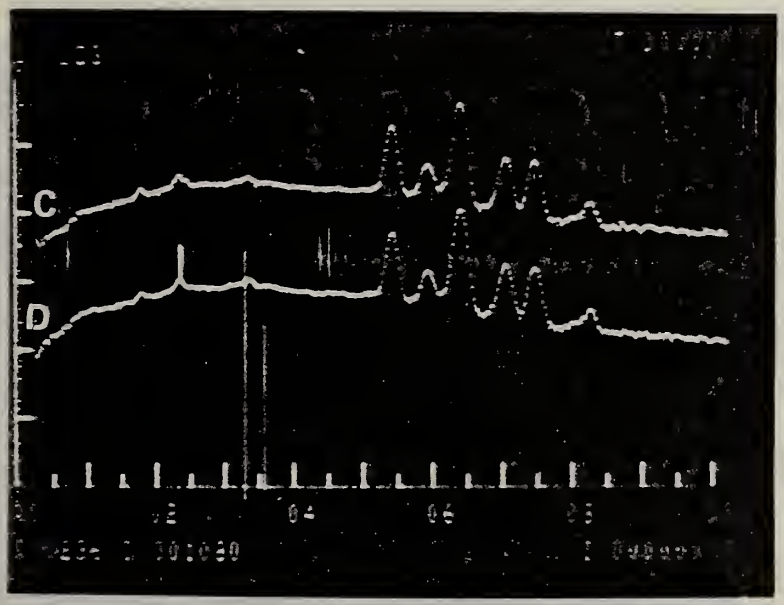

Fig. 6. EDX spectra of regions C and D of Fig. 4 showing bulk spectra.

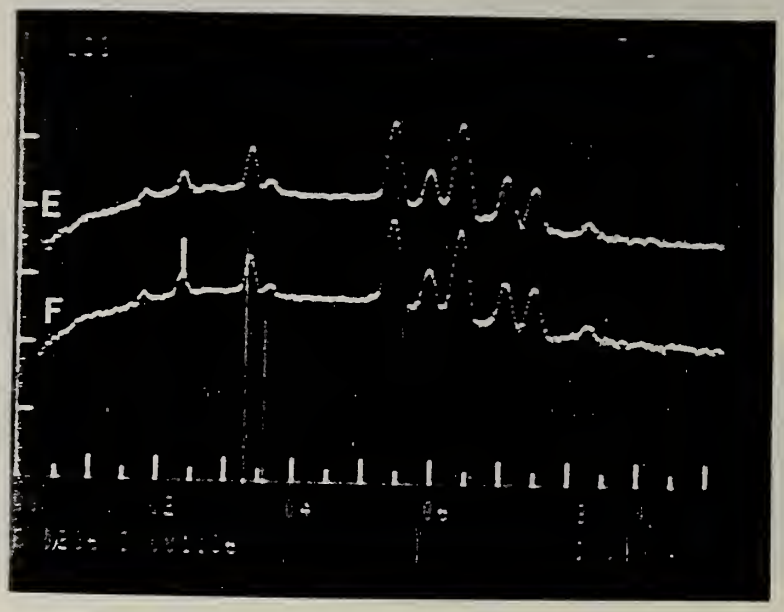

Fig. 7. EDX spectra of regions E and F of Fig. 4 showing high concentrations of Cr.

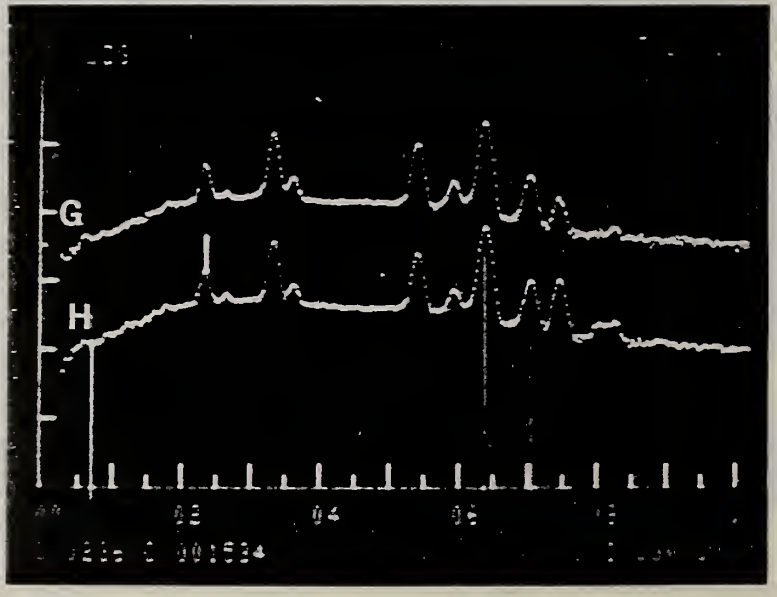

Fig. 8. EDX spectra of regions G and H of Fig. 4 showing low concentration of Ni.

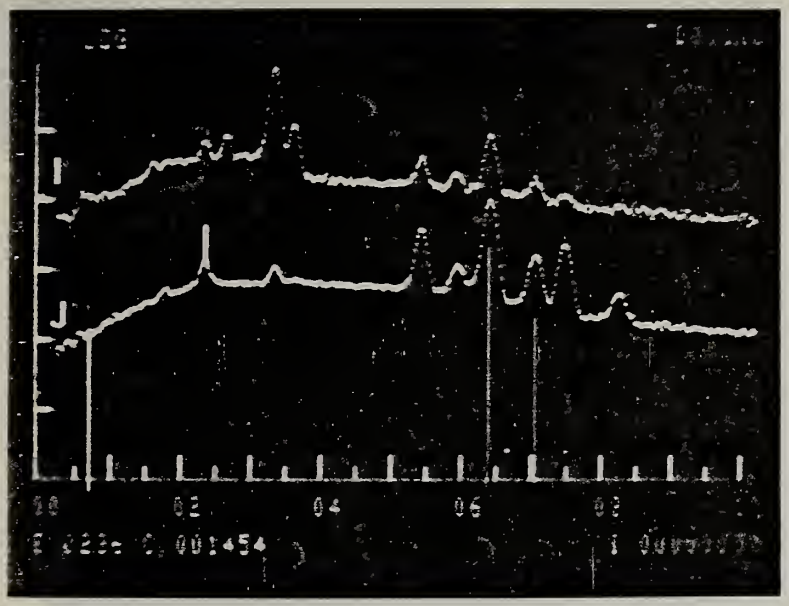

Fig. 9. EDX spectra of regions I and J of Fig. 4 showing high concentrations of K.

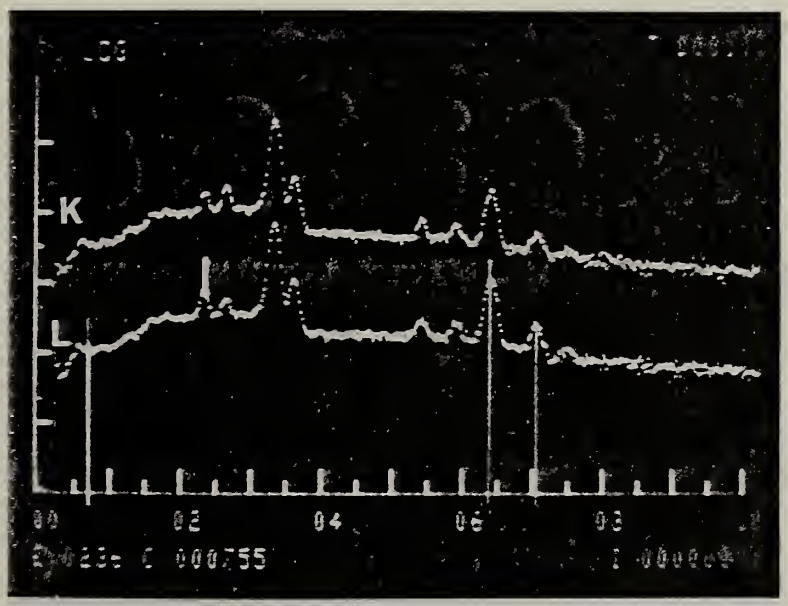

Fig. 10. EDX spectra of regions K and L of Fig. 4 showing high Fe and K concentrations.

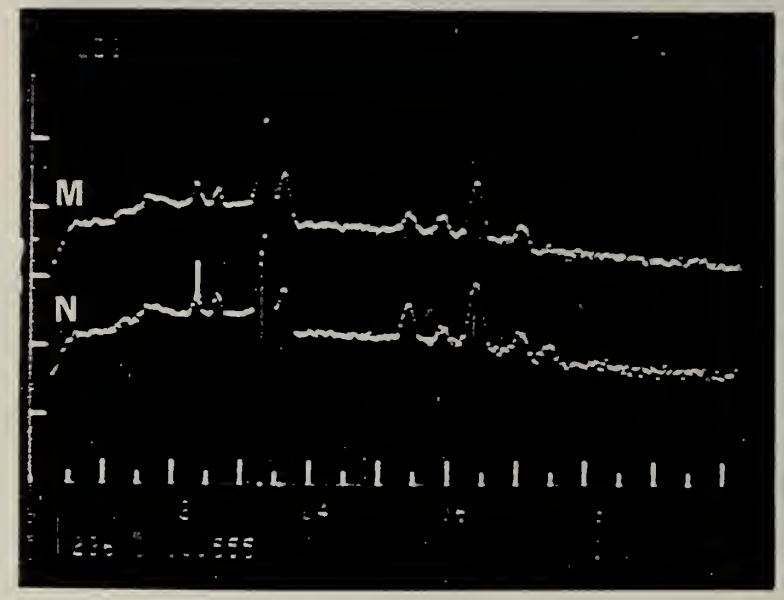

Fig. 11. EDX spectra of regions M and N of Fig. 4 showing high K concentration.

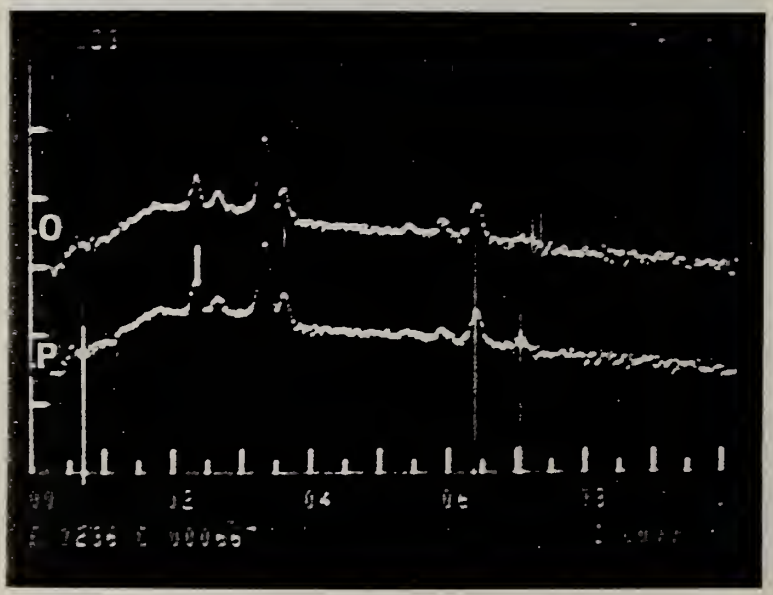

Fig. 12. EDX spectra of regions O and P of Fig. 4 showing Fe and trace Cr in salt deposit.

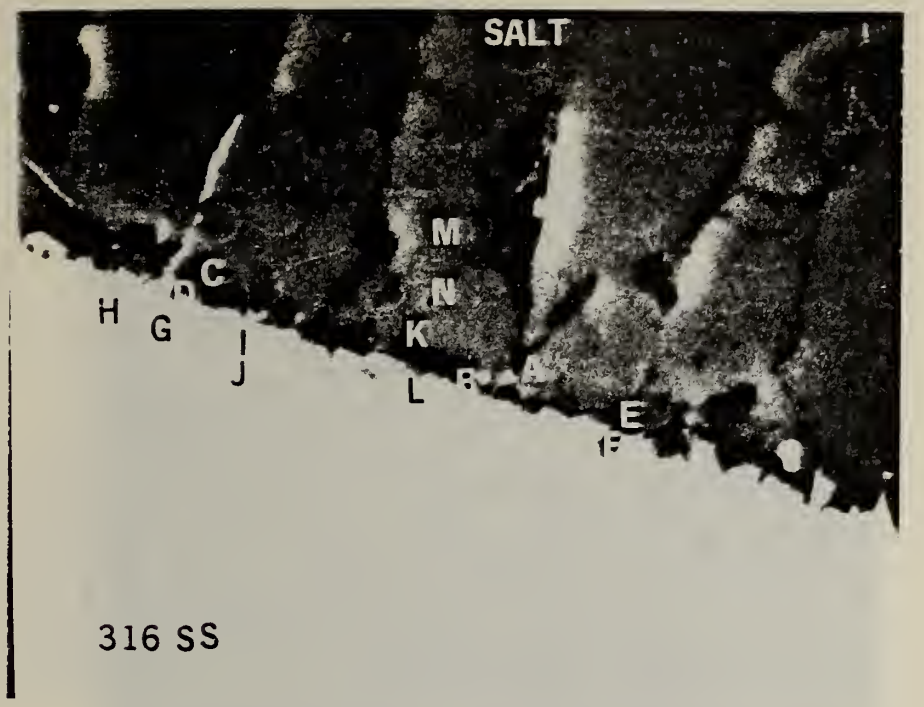

Fig. 13 SEM micrograph, 1800 X, of region T of optical micrograph Fig. 1 showing reaction area at drip zone (fume deposit-salt deposit-metal interface). Lettered regions correspond to labeled EDX spectra, Fig. 14-20.

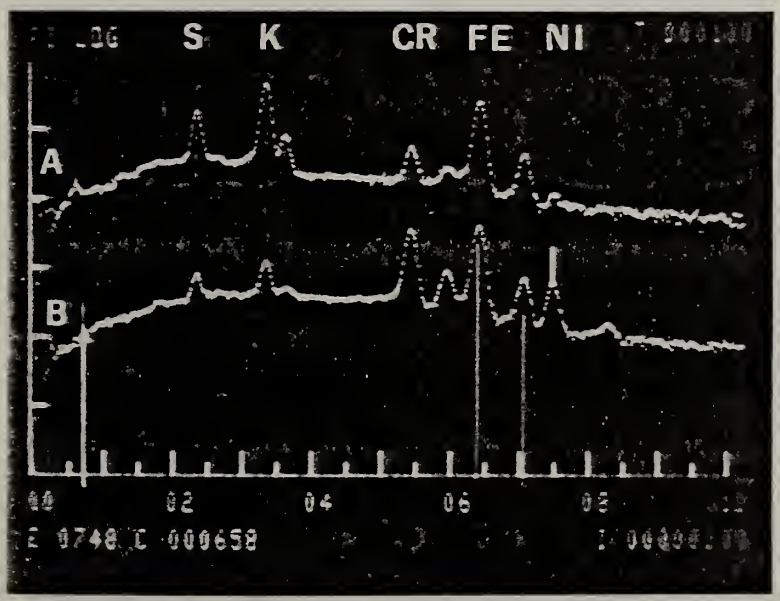

Fig. 14. EDX spectra of regions A and B of Fig. 13 showing high Cr concentration.

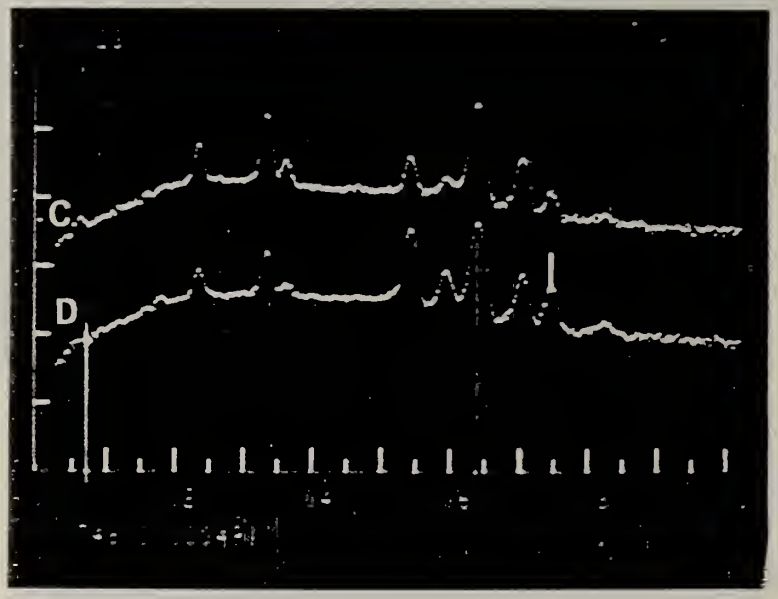

Fig. 15. EDX spectra of regions C and D of Fig. 13 showing high Cr concentration.

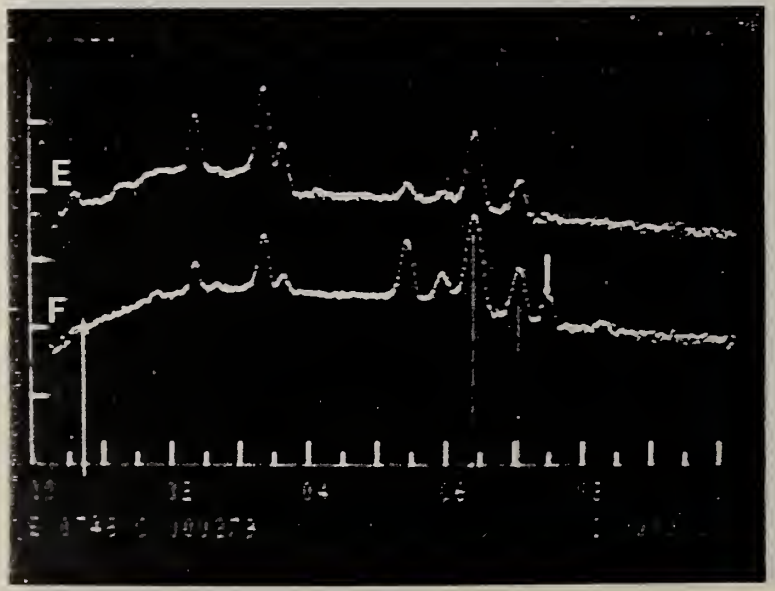

Fig. 16. EDX spectra of regions E and F of Fig. 13 showing high Cr concentration.

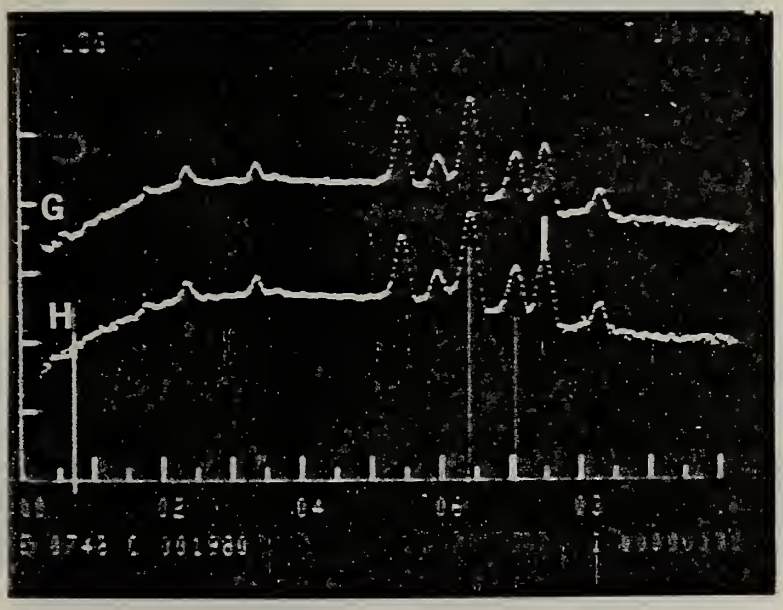

Fig. 17. EDX spectra of regions G and H of Fig. 13 showing high concentrations of both Ni and Cr.

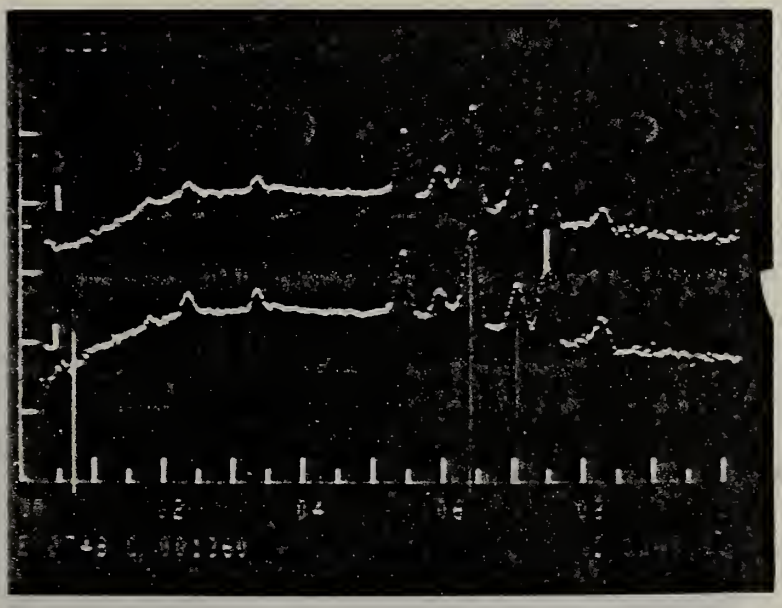

Fig. 18. EDX spectra of regions I and J of Fig. 13 showing high concentrations of both Ni and Cr.

Fig. 19. EDX spectra of regions K and L of Fig. 13 showing high concentrations of both Ni and Cr.

Fig. 20. EDX spectra of regions M and N of Fig. 13 showing high S and K and a trace of Fe.

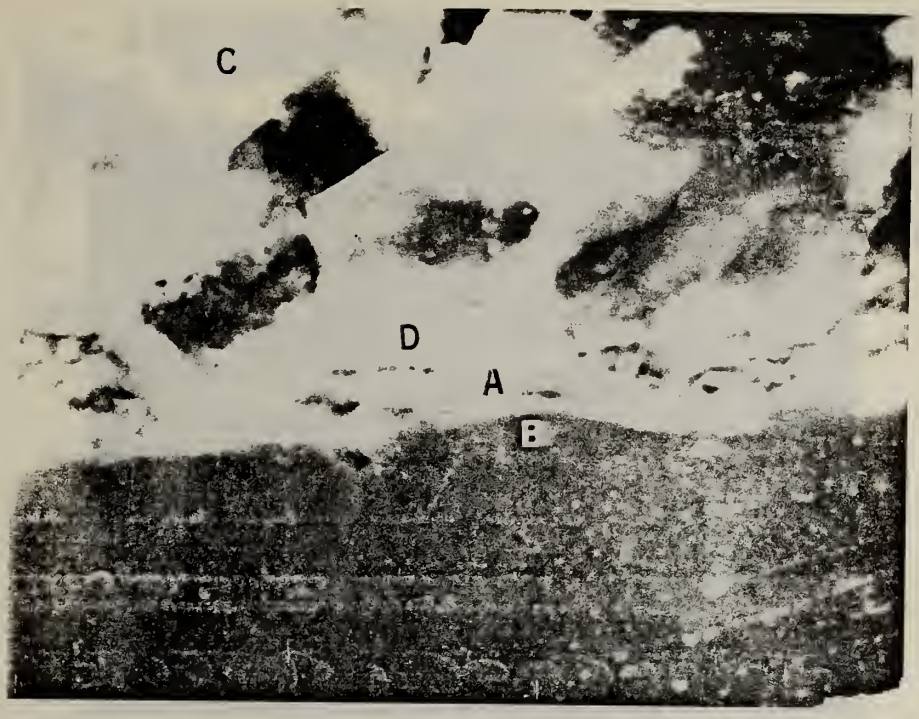

Fig. 21. SEM micrograph, 1800 X, of region Y of optical micrograph Fig. 1 showing reaction area at metal-fume deposit interface. Lettered regions correspond to labeled EDX spectra, Fig. 22 and 23.

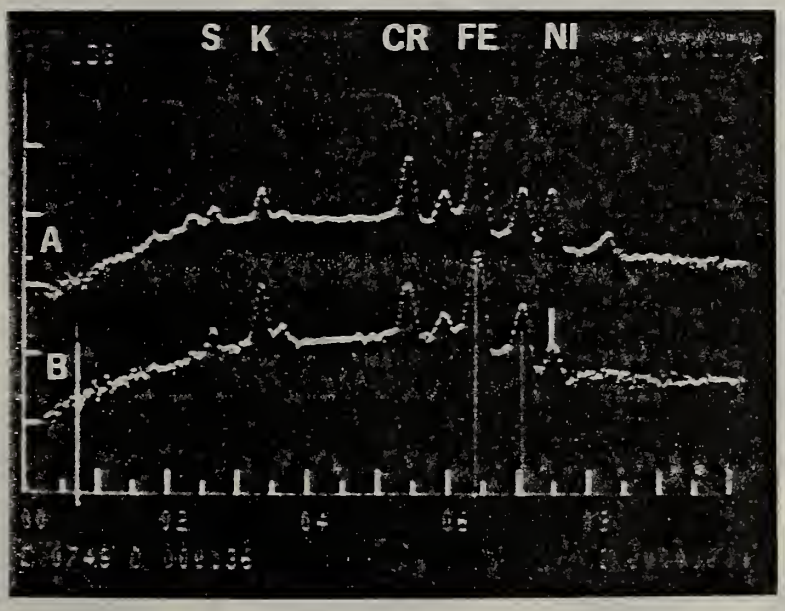

Fig. 22. EDX spectra of regions A and B of Fig. 21 showing high Cr concentrations.

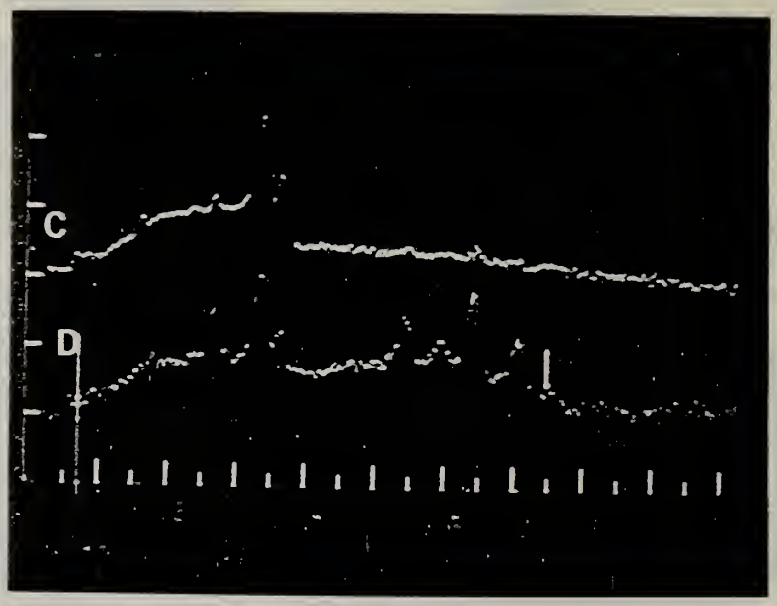

Fig. 23. EDX spectra of regions C and D of Fig. 21 showing absence of Ni.

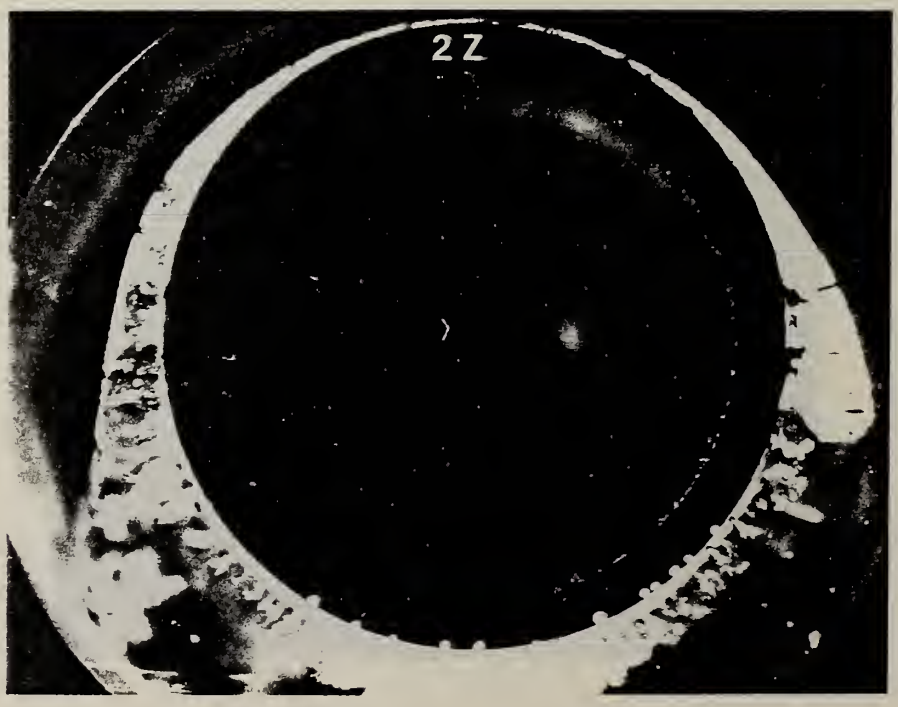

Fig. 24. Optical micrograph of a section of Type 316 stainless steel tubing after exposure to a fuel rich hot gas stream seeded with K_2SO_4 and K_2CO_3. Tube temperature 590°C. Note deposit on upper surface of tube.

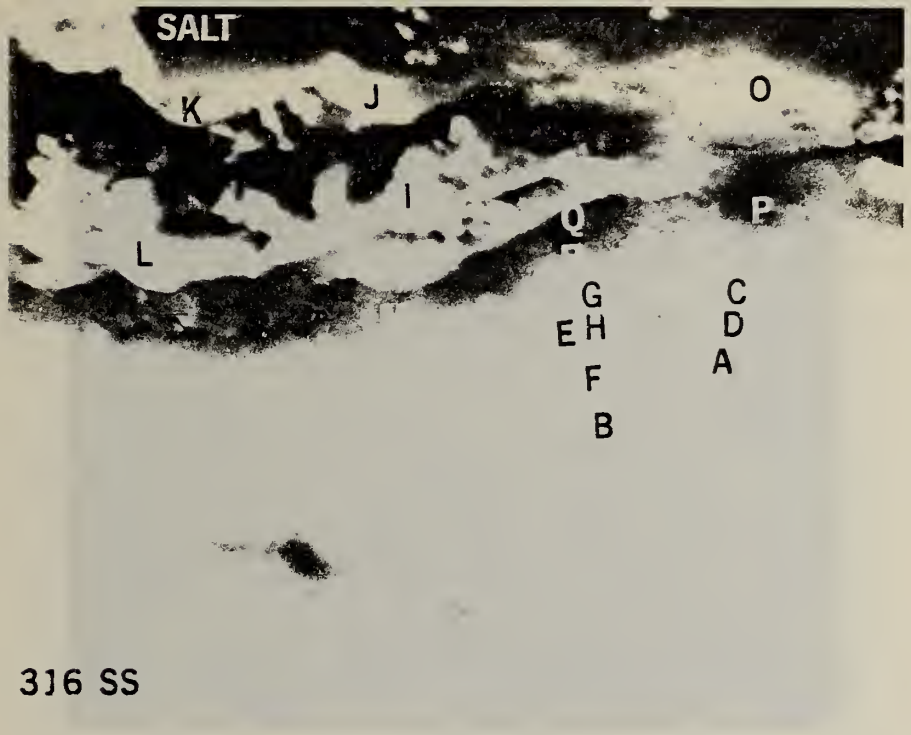

Fig. 25. SEM micrograph, 1720 X, of region 2Z of optical micrograph Fig. 24. Lettered regions correspond to labeled EDX spectra Fig. 26-34.

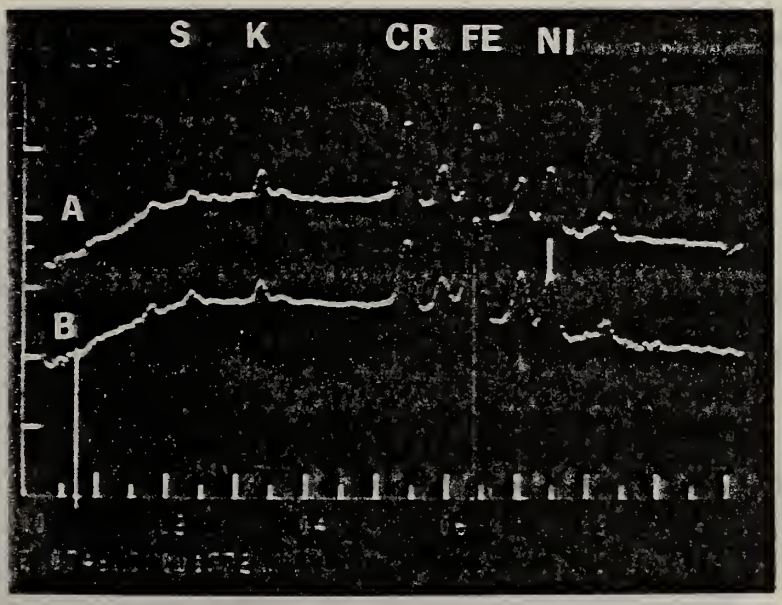

Fig. 26. EDX spectra of regions A and B of Fig. 25 showing high Cr and Ni concentrations.

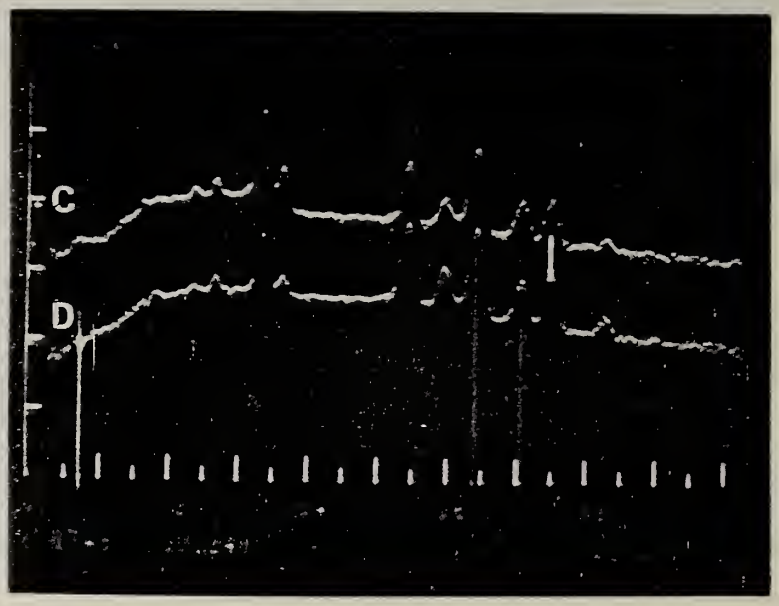

Fig. 27. EDX spectra of regions C and D of Fig. 25 showing high Cr and Ni concentrations.

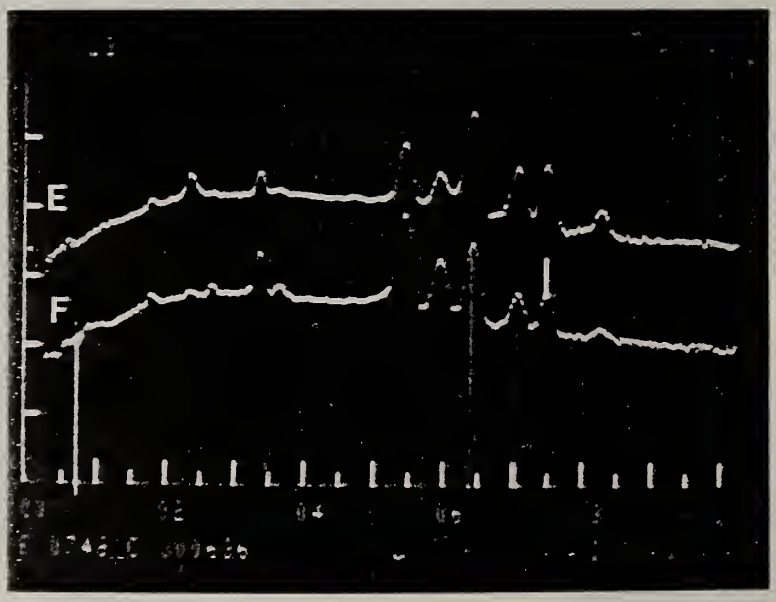

Fig. 28. EDX spectra of regions E and F of Fig. 25 showing high Cr concentrations.

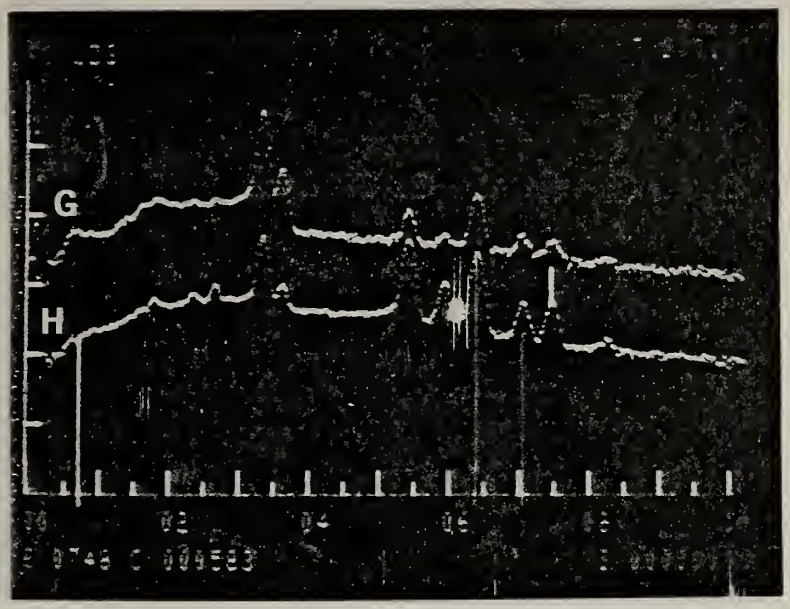

Fig. 29. EDX spectra of regions G and H of Fig. 25 showing high Cr concentrations.

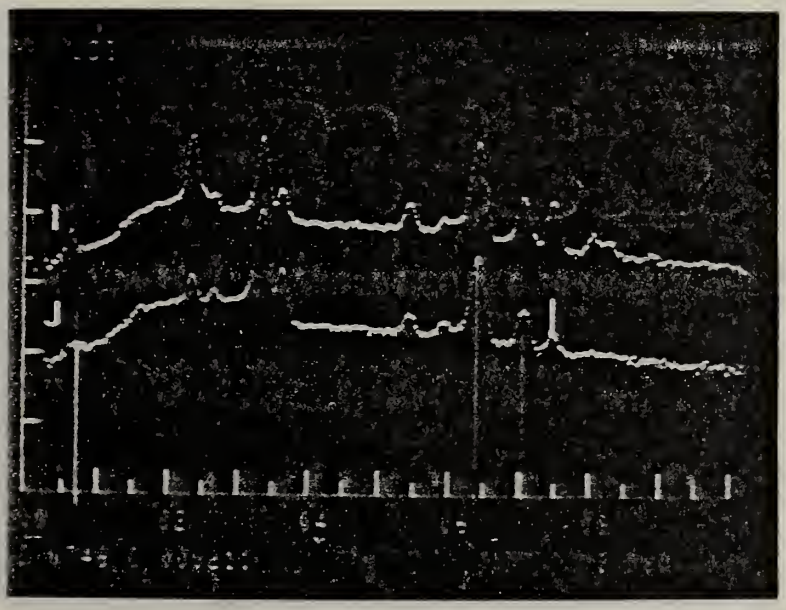

Fig. 30. EDX spectra of regions I and J of Fig. 25 showing high Fe concentrations.

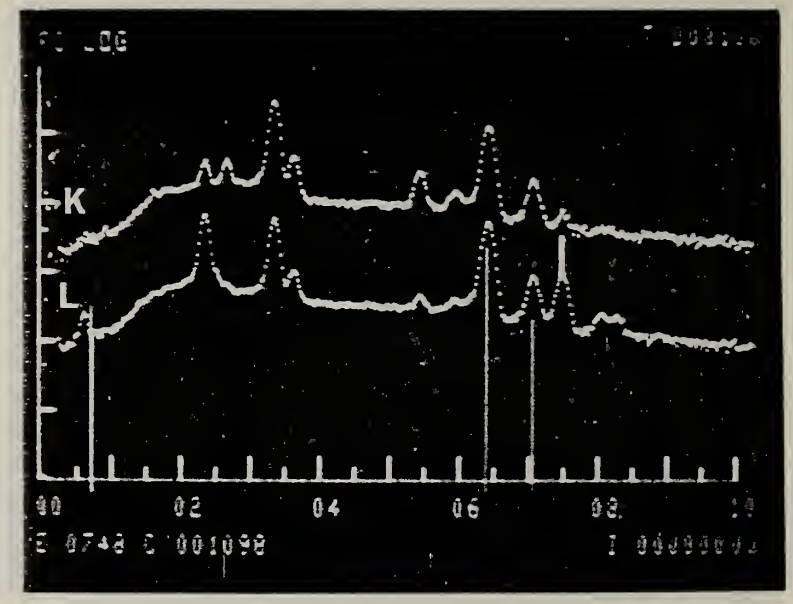

Fig. 31. EDX spectra of regions K and L of Fig. 25 showing high Fe concentrations.

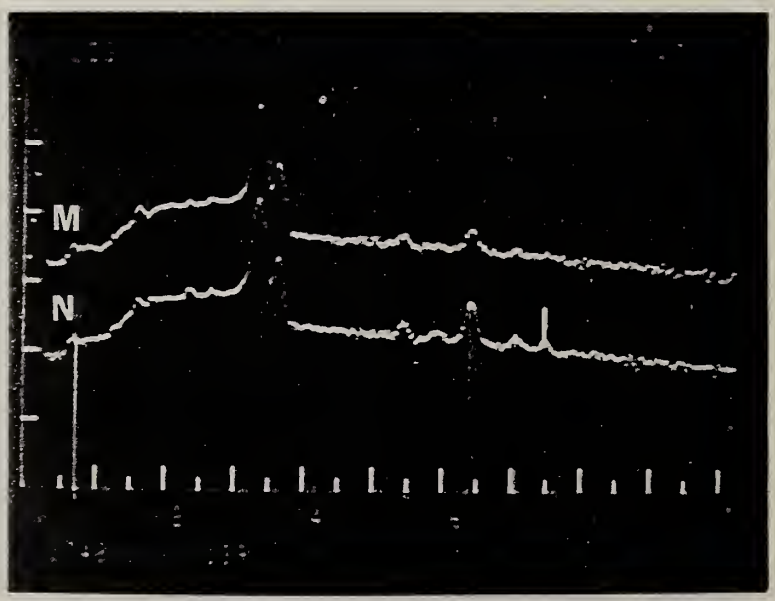

Fig. 32. EDX spectra of regions M and N of Fig. 25 showing Fe.

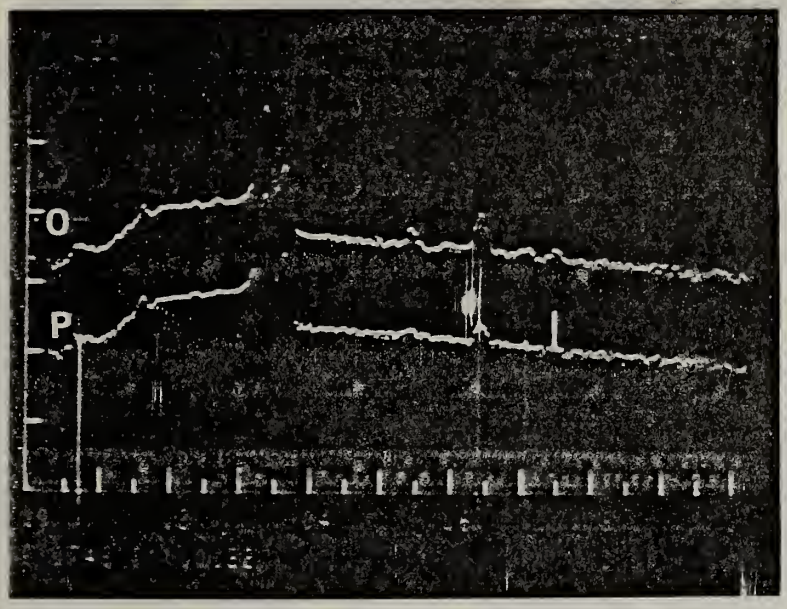

Fig. 33. EDX spectra of regions O and P of Fig. 25 showing trace of Fe in the salt deposit.

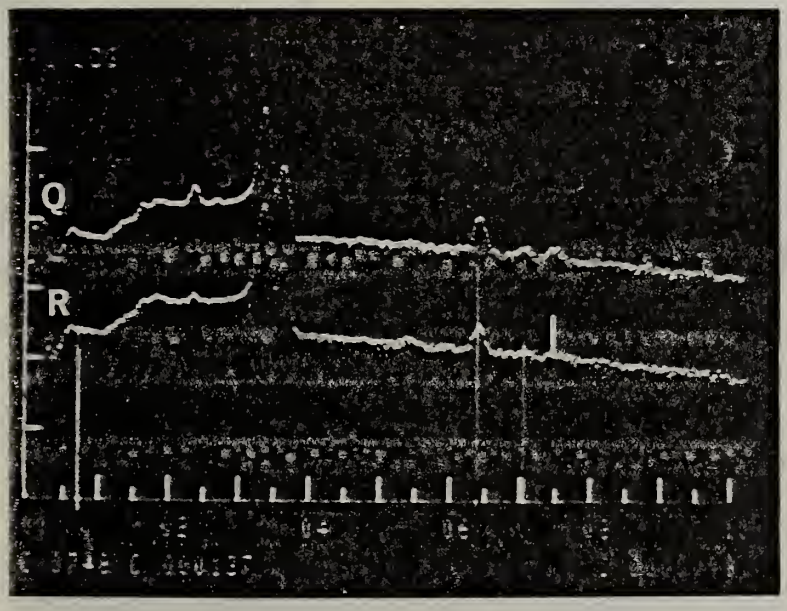

Fig. 34. EDX spectra of regions Q and R of Fig. 25 showing trace of Fe in the salt deposit.

Fig. 35. Optical micrograph of a section of Type 316 stainless steel tubing after exposure to a fuel rich hot gas stream seeded with K_2SO_4. Tube wall temperature 590°C. Note deposit on upper surface of tube.

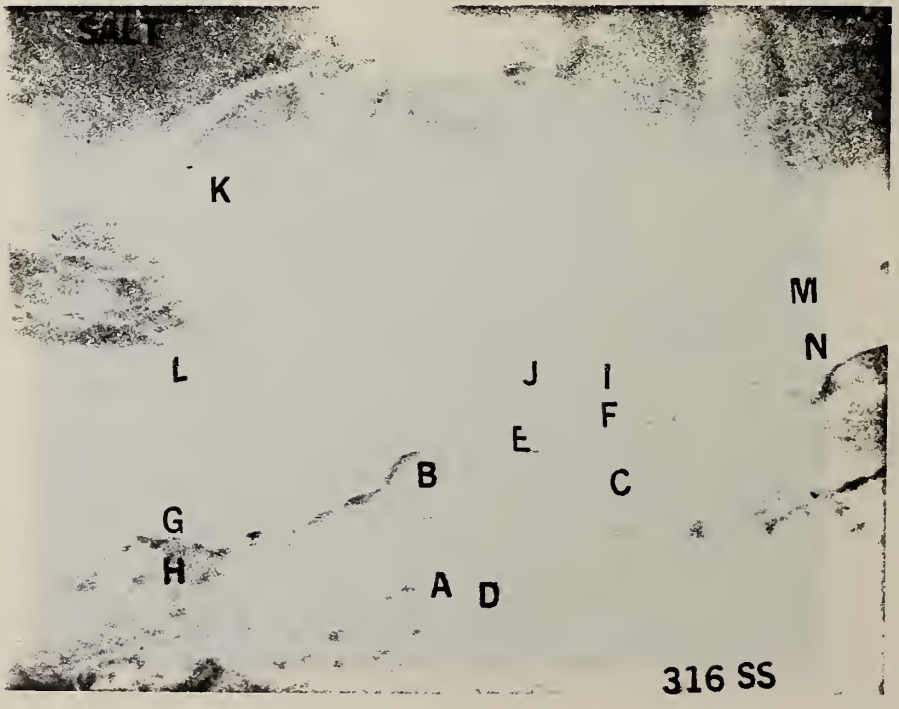

Fig. 36. SEM micrograph, 1720 X, of region 3Z of optical micrograph, Fig. 35. Lettered regions correspond to labeled EDX spectra Fig. 37-43.

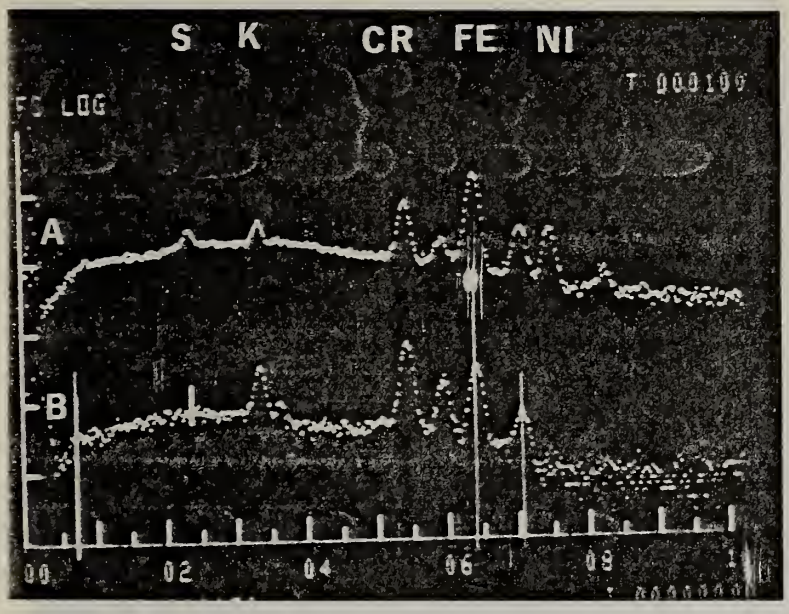

Fig. 37. EDX spectra of regions A and B of Fig. 36 showing high concentrations of Cr and absence of Ni.

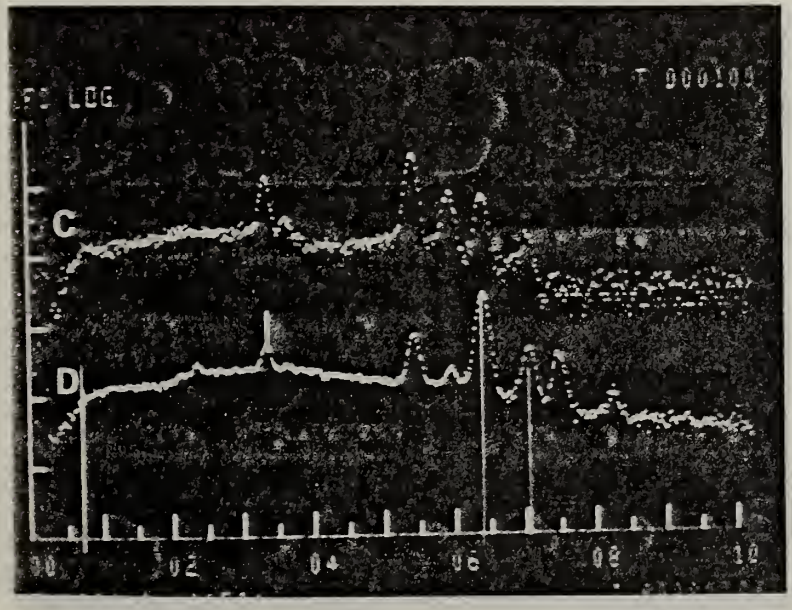

Fig. 38. EDX spectra of regions C and D of Fig. 36 showing high concentrations of Cr and absence of Ni.

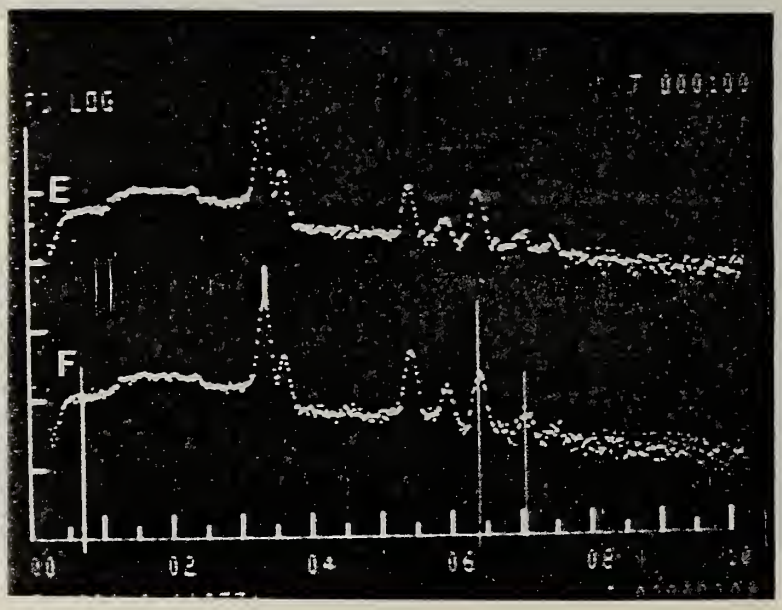

Fig. 39. EDX spectra of regions E and F of Fig. 36 showing high concentrations of Cr and absence of Ni.

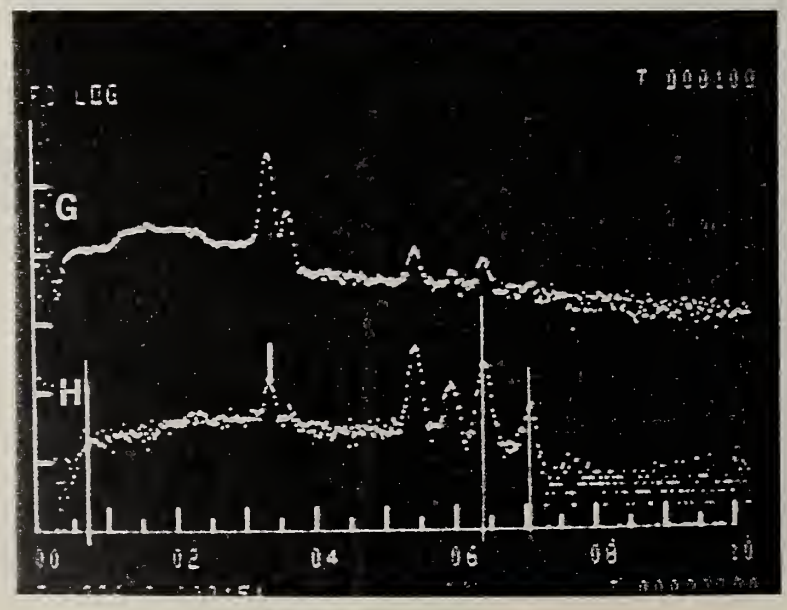

Fig. 40. EDX spectra of regions G and H of Fig. 36 showing high concentrations of Cr and absence of Ni.

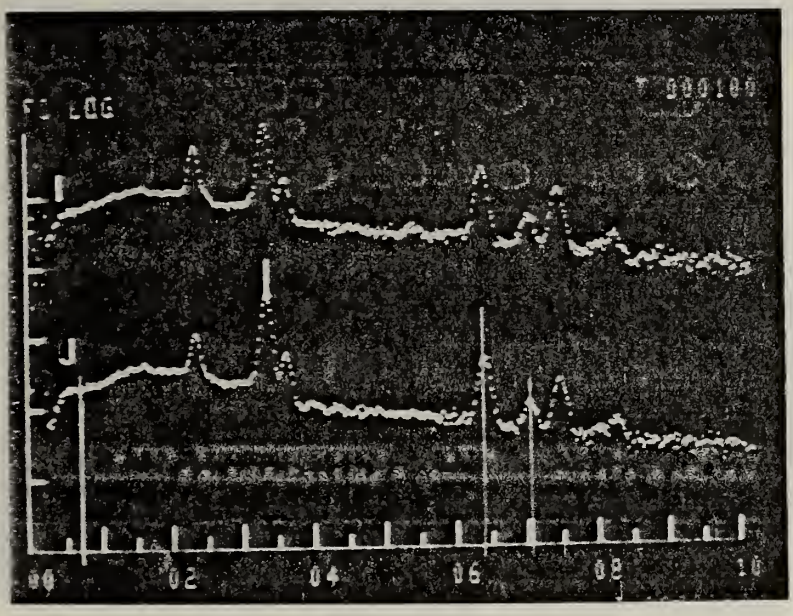

Fig. 41. EDX spectra of regions I and J of Fig. 36 showing high concentrations of Ni and absence of Cr.

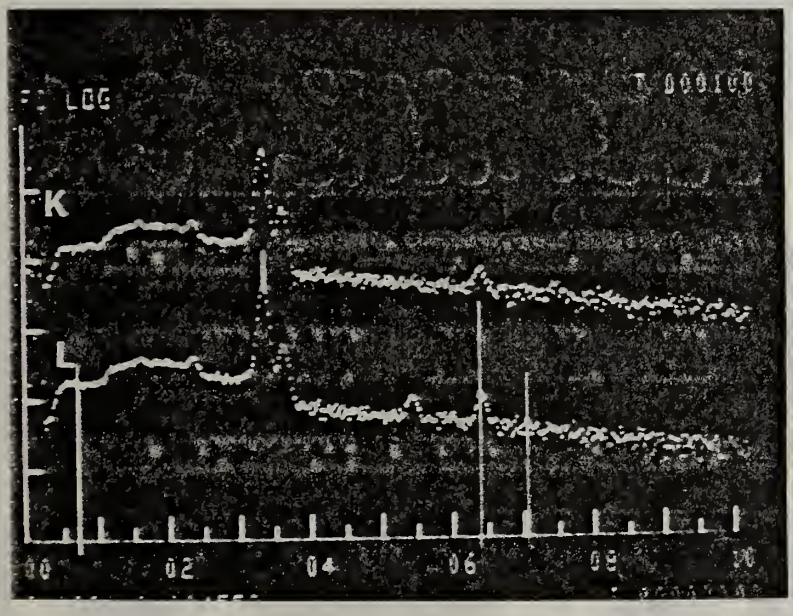

Fig. 42. EDX spectra of regions K and L of Fig. 36 showing high concentrations of K with a trace of Fe and Cr.

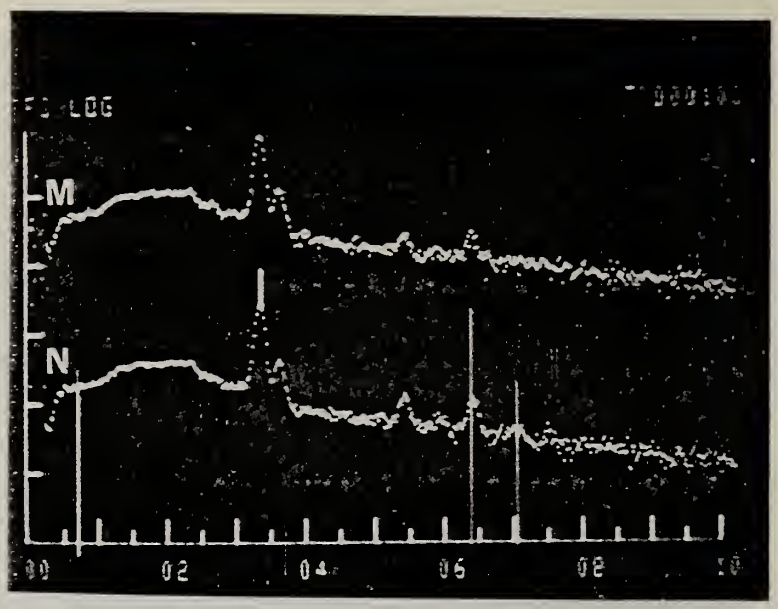

Fig. 43. EDX spectra of regions M and N of Fig. 36 showing high concentrations of K with a trace of Fe and Cr.

Fig. 44. Optical micrograph of a section of Type 316 stainless steel tubing after exposure to a fuel rich hot gas stream seeded with K_2SO_4. Tube wall temperature 500°C. Note deposit on upper surface of tube.

Fig. 45. SEM micrograph, 1160 X, of region 4Z of optical micrograph Fig. 44 showing reaction area at metal-salt interface. Lettered regions correspond to labeled EDX spectra Fig. 46-49.

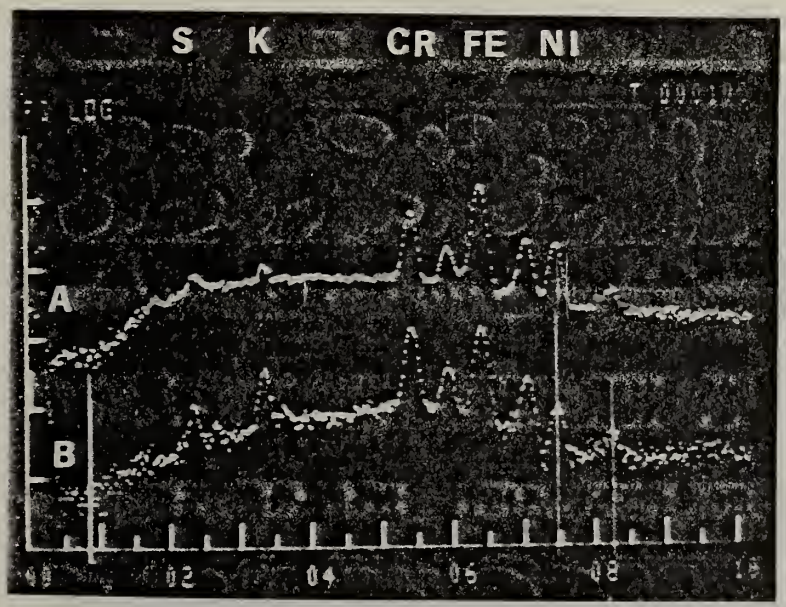

Fig. 46. EDX spectra of regions A and B of Fig. 45 showing high Cr and low Ni concentrations.

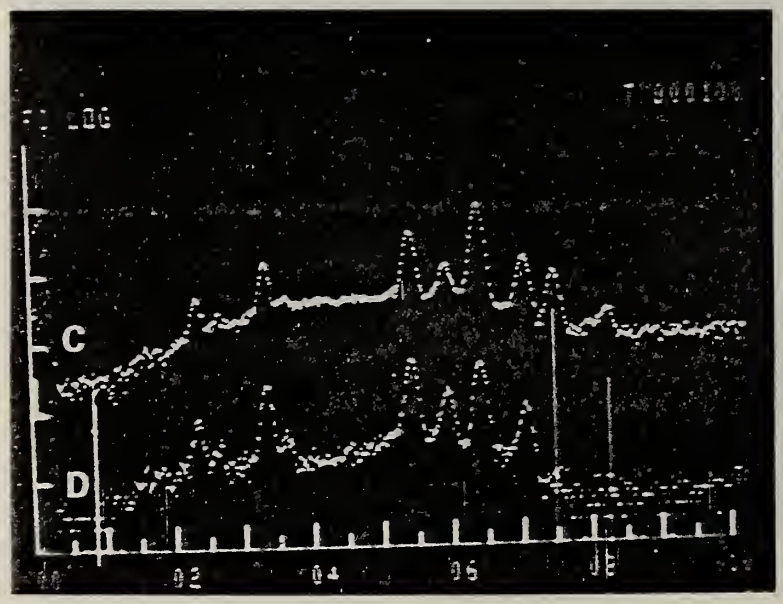

Fig. 47. EDX spectra of regions C and D of Fig. 45 showing high Cr and no Ni.

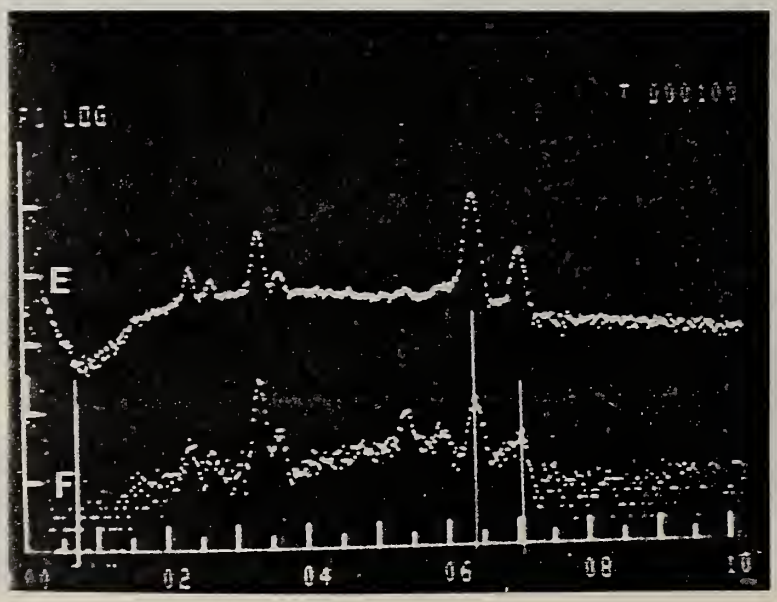

Fig. 48. EDX spectra of regions E and F of Fig. 45 showing high concentrations of Fe with a slight trace of Cr.

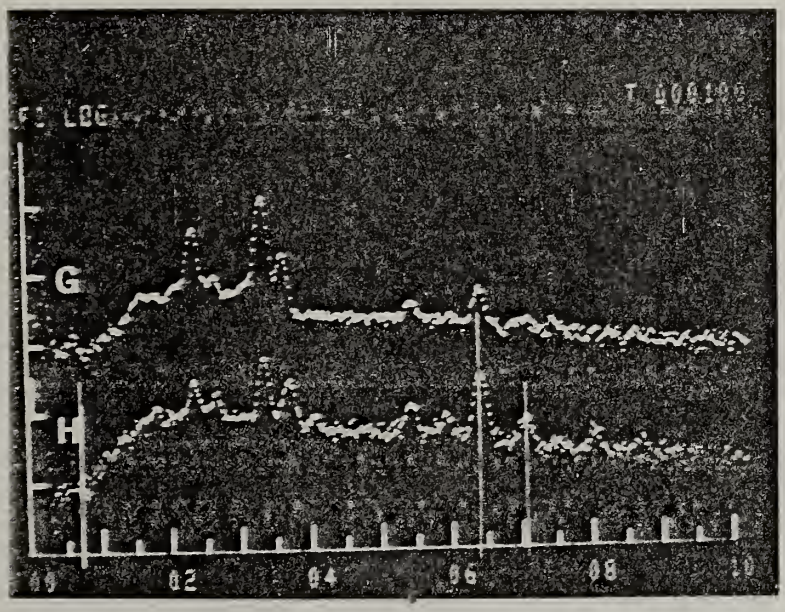

Fig. 49. EDX spectra of regions G and H of Fig. 45 showing Fe with a trace of Cr.